Simplified geotechnical rheological model for simulating viscoelasto-plastic response of ballasted railway substructure

Piyush Punetha, Sanjay Nimbalkar PhD, Hadi Khabbaz PhD

School of Civil and Environmental Engineering, University of Technology Sydney, NSW-2007, Australia

Correspondence

Sanjay Nimbalkar,
School of Civil and Environmental Engineering, University of Technology Sydney, NSW-2007, Australia.
Email: Sanjay.Nimbalkar@uts.edu.au

Abstract

A proper understanding of the mechanical behaviour of the substructure layers is crucial for optimising the design and performance of a ballasted railway track. The recent advent of high-speed trains and heavy haul freight wagons has heightened this need more than ever. The accurate prediction of the long-term performance of the railway tracks under increased speed and loads still remains an intriguing challenge for researchers and design engineers. In this context, the present paper proposes a simplified geotechnical rheological model to evaluate the viscoelasto-plastic response of the track substructure layers. The proposed approach combines plastic slider, elastic springs and viscous dampers to predict the transient response during a train passage, and the irrecoverable deformation accumulated in the track substructure over an operational period. The model simulates tri-layered substructure (ballast, subballast and subgrade) in comparison with existing rheological approaches employing either single or dual-layered substructure. The model is validated against the field data published in the literature. An acceptable agreement between the predicted results and the field data verifies the accuracy of the model. Parametric investigations are conducted to study the influence of train and track parameters on the cumulative track deformation. The results demonstrate the enhanced capability of the rheological model to adequately capture the crucial effects of axle load, train speed and thickness of granular layers on the accumulation of track settlement. The proposed method can provide an effective tool for the practising engineers for quick prediction of changes to the geometry of railway tracks over their operational periods.

KEYWORDS

cumulative deformation, geometry degradation, railway track, rheological model, slider element

1 | INTRODUCTION

The ballasted railway track is the most commonly used track system, which employs multiple layers of geomaterials to transmit the train-induced load into the subgrade soil safely. It constitutes of two major components, substructure and superstructure. The substructure includes geotechnical layers such as ballast, subballast, fill (structural and general) and subgrade (natural and prepared), whose characteristics significantly influence the track response[1]. These layers are conventionally designed using empirical and simplified theoretical approaches that are based on experience with in-service tracks, augmented with extensive laboratory and field testing data[2-4]. Usually, these conventional design approaches lack general applicability in different traffic loading and soil conditions. This serious limitation has recently become more apparent due to a dramatic hike in transportation needs, which has accelerated the deterioration of the existing tracks and incurred significant maintenance costs[5]. Thus, to derive optimum performance from the railway tracks, there is an inevitable need for more reliable, practical and adaptable design method. The development of such a design technique requires a detailed analysis of the mechanical behaviour of track substructure layers and their mutual interaction.

The substructure layers experience both recoverable (elastic) and irrecoverable (plastic) deformations during the train passage. After the initial track settlement, the magnitude of irrecoverable deformation accumulates gradually with an increase in the number of train passages. This cumulative deformation, generated due to repeated train loadings, leads to a loss of track geometry[6-8]. Consequently, the prediction of accumulative permanent deformation in the substructure layers has attracted a great deal of attention. Several researchers have developed empirical models based on extensive field and laboratory investigations to predict the accumulation of irrecoverable deformation in the substructure layers[9-11]. However, these models lack a detailed rational theoretical basis, and their applications are often limited to specific conditions on which they are based. Nevertheless, laboratory tests are often restricted in size due to financial constraints. Meanwhile, the cost and the number of influencing factors in field investigations is too large for accurate parametric studies.

The numerical modelling provides an alternative approach to simulate the track response under the repetitive wheel loads and understand the role of each layer on the overall track response. The behaviour of the ballasted track has been studied in the past using two-dimensional (2D), two-and-a-half dimensional (2.5D) and three-dimensional (3D) finite element (FE) analyses[12-21]. The FE modelling accurately simulates the dynamic behaviour of the railway tracks and the wave propagation phenomenon. However, these models may require relatively large amount of computational resources and time to accurately predict the accumulation of irrecoverable deformation in the substructure layers, especially when the number of load cycles is huge (in the order of millions)[22]. To reduce the computational time required for such analyses, advanced explicit elastoplastic material models[9,23] can be used, which typically require 10-15 input parameters to simulate the behaviour of granular layers accurately.

The analytical modelling technique offers a relatively faster and computationally more efficient alternative to FE analyses for the accurate prediction of track response. Consequently, numerous analytical models with varying degree of complexity have been established to predict the response of the railway track and the surrounding area during train passage[7,24,25]. The track substructure layers in these models are simulated using equivalent springs[26,27], spring-dashpots[28], homogenous[29] or multilayered half-space[30,31], or their combinations[32]. Representing the track layers as an equivalent spring may simulate the overall track behaviour, however, this approach disregards the interaction among the substructure layers. Some researchers addressed this issue by modelling the substructure layers as lumped masses connected using visco-elastic elements, such as springs and dashpots[33-36]. A few studies have also considered the substructure layers as an assemblage of discrete particles. Suiker et al.[37] modelled the ballast as a layer of discrete particles that are mutually connected by elastic longitudinal and shear springs, and studied the propagation of body wave through this layer. In a similar study, Suiker et al.[38] investigated the steady-state response of the ballast layer composed of discrete particles to a moving, harmonically vibrating load. Most of these studies investigated the transient response of the tracks during train passage and research regarding the prediction of settlement accumulated in the substructure layers over a specified period or tonnage is still very limited.

This study attempts to evaluate the mechanical response of the ballasted track substructure layers using a simplified geotechnical rheological model. The proposed model can predict both the transient response during a train passage and the irrecoverable deformations accumulated over a specified period or tonnage. The elastic response is represented using elastic springs, while the viscous response is captured through dashpots (or dampers). The plastic (or irrecoverable) response is simulated using the slider elements. The first part of the article describes the viscoelasto-plastic model formulation and the second part illustrates its validation against published field investigation data. Subsequently, a parametric investigation is carried out to study the influence of train and track parameters on the cumulative deformation. The purpose of this study is to provide a simple geotechnical rheological technique that can be used for a quick evaluation of the track substructure response under repeated traffic loadings.

2 | MODEL DESCRIPTION

The evaluation of track response in the present approach is carried out in two parts. Firstly, the calculation of the train-induced load transmitted to the substructure layers is presented. This part employs a relatively simple mathematical expression, which describes the load with a reasonable degree of accuracy. In the second part, the transient and irrecoverable response of the track layers is predicted using a viscoelasto-plastic geotechnical rheological model.

2.1 | Determination of load

In ballasted railway tracks, the vertical load imposed on the substructure layers is transferred from the superstructure via the sleeper-ballast (or tie-ballast) contact. This load is equal to the vertical rail seat load and can be evaluated by applying the beam on elastic foundation (BoEF) approach. This technique is often used to evaluate the rail seat load owing to simplicity and reasonably accurate predictions[39]. The Australian standard AS 1085.14[40] also recommends the use of the BoEF approach to estimate the proportion of axle/wheel load transferred to individual sleepers.

In this method, the vertical rail seat load (Q_r) is calculated as the product of sleeper spacing (S_s), vertical track deflection (w) and the track modulus (k) (i.e., $S_s \times w \times k$)[39]. The vertical track deflection is calculated using the following equation[7]:

$$w(x) = \frac{Q}{2kL} e^{-\frac{x}{L}} \left[\cos\left(\frac{x}{L}\right) + \sin\left(\frac{x}{L}\right)\right] \quad (1)$$

in which $w(x)$ is the vertical track deflection (m) at a distance of x (m) along the longitudinal direction of the track (i.e., the direction of train movement); Q is the static wheel load (N); k is the track modulus (N/m^2); L is the characteristic length (m) [$L=(4E_rI_r/k)^{1/4}$]; E_r and I_r are Young's modulus (N/m^2) and moment of inertia (m^4) of the rail, respectively.

As the train wheel moves over the railway track, the vertical deflection at a particular sleeper location varies. Consequently, the vertical rail seat load at each sleeper position fluctuates with time, depending on the location of the wheel with respect to sleeper at a particular time instant. The effect of the series of moving wheels of a train is addressed by using the superposition principle as:

$$Q_{\mathrm{r,n}}(t) = kS_{\mathrm{s}} \sum_{j=1}^{a_{\mathrm{t}}} w(x_{\mathrm{n}}^{j}, t) \quad (2)$$

where $Q_{r,n}$ is the vertical rail seat load at n^{th} sleeper; x_n^j is the distance of the n^{th} sleeper from the j^{th} wheel; a_t is the number of wheels or axles considered. The track modulus in Equations (1) and (2), can either be determined using field measurements on the railway track[41] or can be calculated using a theoretical approach[39]. In the theoretical approach, the track modulus is evaluated by dividing the system support stiffness[42] with the sleeper spacing. The system support stiffness (k_t) is evaluated as the series equivalent of the stiffness of the rail pad (k_p), ballast (k_b), subballast (k_s) and subgrade (k_g) layers[36].

$$\frac{1}{k_{\mathrm{t}}} = \left(\frac{1}{k_{\mathrm{p}}} + \frac{1}{k_{\mathrm{b}}} + \frac{1}{k_{\mathrm{s}}} + \frac{1}{k_{\mathrm{g}}}\right) \tag{3}$$

Figure 1 shows the deflection profile below the train wheels, calculated using Equation (1), at time instant t_1. The total deflection below each sleeper due to multiple wheels, at each time instant, can be calculated using the superposition principle. The resultant deflection profile is represented using dashed lines in Figure 1. After evaluating the total deflection, the vertical rail seat load (or sleeper reaction) at each time instant can be determined by employing Equation (2) for all the sleepers under consideration (25 in the present study). Similarly, the entire load-time history during the passage of all the wheels of a train can be calculated for all the sleepers.

To assess the suitability of this approach, the predicted rail seat load-time history is compared with the data recorded in the field measurements. Figure 2 depicts a comparison of the rail seat load predicted using the present method with the field data reported by Mishra et al.[43] during the passage of the Acela Express passenger train. The rail seat load or sleeper reaction, in the field, was calculated by subtracting the wheel load measured at sleeper location (Figure 2b) from that measured between adjacent sleepers (Figure 2a)[44]. It can be observed that the rail seat load-time history predicted using the present method is in an acceptable agreement with the in-situ measurements (Figure 2c). Therefore, this method can accurately predict the load transmitted to the track substructure layers during the train passage.

2.1.1 | Stress distribution

The stress distribution below a sleeper is calculated using the Boussinesq solutions for a uniformly loaded circular footing[45-47]. However, the Boussinesq approach considers the substructure as an isotropic elastic homogenous medium in contrast to the actual layered structure. An approximate solution to this problem is the theory of equivalent thickness proposed by Palmer and Barber[48] and Odemark[49], which transforms the multiple layers of soil, such as ballast and subballast, into an equivalent thickness of a single layer material. Using this theory, the equivalent thickness of the ballast (h_{eb}) and subballast (h_{es}) layers can be determined by[50]:

$$h_{\mathrm{eb}} = \begin{cases} h_{\mathrm{b}} \left[\dfrac{E_{\mathrm{b}}\left(1-\nu_{\mathrm{g}}^{2}\right)}{E_{\mathrm{g}}\left(1-\nu_{\mathrm{b}}^{2}\right)} \right]^{\frac{1}{3}}, & E_{\mathrm{b}} > E_{\mathrm{g}} \\ h_{\mathrm{b}} \left\langle 0.75 + 0.25 \left[\dfrac{E_{\mathrm{b}}\left(1-\nu_{\mathrm{g}}^{2}\right)}{E_{\mathrm{g}}\left(1-\nu_{\mathrm{b}}^{2}\right)} \right]^{\frac{1}{3}} \right\rangle, & E_{\mathrm{b}} < E_{\mathrm{g}} \end{cases} \tag{4}$$

$$h_{\mathrm{es}} = \begin{cases} h_{\mathrm{s}} \left[\dfrac{E_{\mathrm{s}}\left(1-\nu_{\mathrm{g}}^{2}\right)}{E_{\mathrm{g}}\left(1-\nu_{\mathrm{s}}^{2}\right)} \right]^{\frac{1}{3}}, & E_{\mathrm{s}} > E_{\mathrm{g}} \\ h_{\mathrm{s}} \left\langle 0.75 + 0.25 \left[\dfrac{E_{\mathrm{s}}\left(1-\nu_{\mathrm{g}}^{2}\right)}{E_{\mathrm{g}}\left(1-\nu_{\mathrm{s}}^{2}\right)} \right]^{\frac{1}{3}} \right\rangle, & E_{\mathrm{s}} < E_{\mathrm{g}} \end{cases} \tag{5}$$

where the subscripts *b*, *s* and *g* denote the ballast, subballast and subgrade layers, respectively; *E*, *h* and *v* are Young's modulus (N/m^2), thickness (m) and Poisson's ratio of the substructure layers, respectively. Thus, the stress distribution is determined by assuming the sleeper-ballast contact pressure, below each rail seat, to be uniformly distributed over a circular area whose size is related to the sleeper dimensions [as shown in APPENDIX-1 (Figure A1)]. A similar assumption has been used in past studies for the sleeper-ballast contact pressure [e.g., Love's equation[1]].

2.2 | Prediction of the track response

The substructure of the ballasted railway tracks comprises of multiple layers of granular materials which undergo both recoverable and irrecoverable deformations under the application of repeated traffic loadings[51]. In the present approach, the recoverable and irrecoverable response of the substructure layers is predicted using a geotechnical rheological model. Three substructure layers have been considered, which include ballast, subballast and subgrade. The model employs elastic and viscous elements, such as springs and dashpots, to represent the visco-elastic response while the slider elements capture the irrecoverable response of the substructure layers.

Figure 3 presents the geotechnical rheological model of the track used in this study. One half of the track is modelled due to the symmetry with respect to the track's centreline. The interfaces between the substructure layers (ballast-subballast and subballast-subgrade interfaces) are considered as rigid, i.e., no slippage is allowed between the layers. The track substructure layers are represented as discrete masses that are connected using elastic springs, viscous dampers (or dashpots) and plastic slider elements, as shown in Figure 3. As the loading commences, the springs and dampers deform visco-elastically while the plastic slider elements remain fixed. Once the stress state in the substructure layers reaches the yield surface (defined by f_b, f_s and f_g for ballast, subballast and subgrade, respectively), the slider elements start moving. During unloading, the springs and dampers deform, however, the plastic slider element does not move. When the track is reloaded, the springs and dampers deform whereas the slider element moves only if the stress state reaches the yield surface. Thus, the movement of the slider element is irrecoverable, and it accumulates with an increase in the number of load repetitions. The amount by which the slider element moves during a loading stage can be described by using an appropriate constitutive relationship, which is discussed later in section 2.2.2.

Thus, the total displacement in each substructure layer of the track can be decomposed into a recoverable part (viscoelastic) and an irrecoverable part (plastic) as:

$$z_g(t) = z_g^{ve}(t) + z_g^{p}(t);\; z_s(t) = z_g(t) + z_s^{ve}(t) + z_s^{p}(t);\; z_b(t) = z_s(t) + z_b^{ve}(t) + z_b^{p}(t) \quad (6)$$

where the superscript *ve* and *p* represent the visco-elastic and plastic components of the response, respectively; z_b, z_s and z_g denote the total vertical displacement in the ballast, subballast and subgrade layers, respectively. In this equation, the initiation and evolution of the plastic displacement in the substructure layers can be described by using an appropriate constitutive relationship, which is discussed later in section 2.2.2.

2.2.1 | Equations of motion for the track layers

On applying the dynamic equilibrium condition in the rheological model shown in Figure 3, the following system of equations in the incremental form can be derived:

$$
\begin{aligned}
&\begin{bmatrix} m_{\mathrm{g}} & 0 & 0 \\ 0 & m_{\mathrm{s}} & 0 \\ 0 & 0 & m_{\mathrm{b}} \end{bmatrix}\begin{Bmatrix} d\ddot{z}_{\mathrm{g,n}} \\ d\ddot{z}_{\mathrm{s,n}} \\ d\ddot{z}_{\mathrm{b,n}} \end{Bmatrix} + \begin{bmatrix} c_{\mathrm{g}} + c_{\mathrm{s}} + 2c_{\mathrm{g}}^{s} & -c_{\mathrm{s}} & 0 \\ -c_{\mathrm{s}} & c_{\mathrm{s}} + c_{\mathrm{b}} + 2c_{\mathrm{s}}^{s} & -c_{\mathrm{b}} \\ 0 & -c_{\mathrm{b}} & c_{\mathrm{b}} + 2c_{\mathrm{b}}^{s} \end{bmatrix}\begin{Bmatrix} d\dot{z}_{\mathrm{g,n}} \\ d\dot{z}_{\mathrm{s,n}} \\ d\dot{z}_{\mathrm{b,n}} \end{Bmatrix} \\
&+ \begin{bmatrix} k_{\mathrm{g}} + k_{\mathrm{s}} + 2k_{\mathrm{g}}^{s} & -k_{\mathrm{s}} & 0 \\ -k_{\mathrm{s}} & k_{\mathrm{s}} + k_{\mathrm{b}} + 2k_{\mathrm{s}}^{s} & -k_{\mathrm{b}} \\ 0 & -k_{\mathrm{b}} & k_{\mathrm{b}} + 2k_{\mathrm{b}}^{s} \end{bmatrix}\begin{Bmatrix} dz_{\mathrm{g,n}} \\ dz_{\mathrm{s,n}} \\ dz_{\mathrm{b,n}} \end{Bmatrix} \\
&+ \begin{bmatrix} -k_{\mathrm{g}} - 2k_{\mathrm{g}}^{s} & k_{\mathrm{s}} & 0 \\ -2k_{\mathrm{s}}^{s} & -k_{\mathrm{s}} - 2k_{\mathrm{s}}^{s} & k_{\mathrm{b}} \\ -2k_{\mathrm{b}}^{s} & -2k_{\mathrm{b}}^{s} & -k_{\mathrm{b}} - 2k_{\mathrm{b}}^{s} \end{bmatrix}\begin{Bmatrix} dz_{\mathrm{g,n}}^{p} \\ dz_{\mathrm{s,n}}^{p} \\ dz_{\mathrm{b,n}}^{p} \end{Bmatrix} \\
&+ \begin{bmatrix} -c_{\mathrm{g}} - 2c_{\mathrm{g}}^{s} & c_{\mathrm{s}} & 0 \\ -2c_{\mathrm{s}}^{s} & -c_{\mathrm{s}} - 2c_{\mathrm{s}}^{s} & c_{\mathrm{b}} \\ -2c_{\mathrm{b}}^{s} & -2c_{\mathrm{b}}^{s} & -c_{\mathrm{b}} - 2c_{\mathrm{b}}^{s} \end{bmatrix}\begin{Bmatrix} d\dot{z}_{\mathrm{g,n}}^{p} \\ d\dot{z}_{\mathrm{s,n}}^{p} \\ d\dot{z}_{\mathrm{b,n}}^{p} \end{Bmatrix} \\
&= \begin{Bmatrix} dF_{\mathrm{g,n}} \\ dF_{\mathrm{s,n}} \\ dF_{\mathrm{b,n}} \end{Bmatrix} + \begin{bmatrix} c_{\mathrm{g}}^{s} & 0 & 0 \\ 0 & c_{s}^{s} & 0 \\ 0 & 0 & c_{\mathrm{b}}^{s} \end{bmatrix}\begin{Bmatrix} d\dot{z}_{\mathrm{g,n+1}} + d\dot{z}_{\mathrm{g,n-1}} \\ d\dot{z}_{\mathrm{s,n+1}} + d\dot{z}_{\mathrm{s,n-1}} \\ d\dot{z}_{\mathrm{b,n+1}} + d\dot{z}_{\mathrm{b,n-1}} \end{Bmatrix} + \begin{bmatrix} k_{\mathrm{g}}^{s} & 0 & 0 \\ 0 & k_{\mathrm{s}}^{s} & 0 \\ 0 & 0 & k_{\mathrm{b}}^{s} \end{bmatrix}\begin{Bmatrix} dz_{\mathrm{g,n+1}} + dz_{\mathrm{g,n-1}} \\ dz_{\mathrm{s,n+1}} + dz_{\mathrm{s,n-1}} \\ dz_{\mathrm{b,n+1}} + dz_{\mathrm{b,n-1}} \end{Bmatrix} \\
&- \begin{bmatrix} c_{\mathrm{g}}^{s} & 0 & 0 \\ c_{\mathrm{s}}^{s} & c_{\mathrm{s}}^{s} & 0 \\ c_{\mathrm{b}}^{s} & c_{\mathrm{b}}^{s} & c_{\mathrm{b}}^{s} \end{bmatrix}\begin{Bmatrix} d\dot{z}_{\mathrm{g,n+1}}^{p} + d\dot{z}_{\mathrm{g,n-1}}^{p} \\ d\dot{z}_{\mathrm{s,n+1}}^{p} + d\dot{z}_{\mathrm{s,n-1}}^{p} \\ d\dot{z}_{\mathrm{b,n+1}}^{p} + d\dot{z}_{\mathrm{b,n-1}}^{p} \end{Bmatrix} - \begin{bmatrix} k_{\mathrm{g}}^{s} & 0 & 0 \\ k_{\mathrm{s}}^{s} & k_{\mathrm{s}}^{s} & 0 \\ k_{\mathrm{b}}^{s} & k_{\mathrm{b}}^{s} & k_{\mathrm{b}}^{s} \end{bmatrix}\begin{Bmatrix} dz_{\mathrm{g,n+1}}^{p} + dz_{\mathrm{g,n-1}}^{p} \\ dz_{\mathrm{s,n+1}}^{p} + dz_{\mathrm{s,n-1}}^{p} \\ dz_{\mathrm{b,n+1}}^{p} + dz_{\mathrm{b,n-1}}^{p} \end{Bmatrix}
\end{aligned}
\tag{7}
$$

where the subscripts *b*, *s* and *g* stand for the ballast, subballast and subgrade layers, respectively; the subscripts *n*, *n*–1 and *n*+1 denote the n^{th}, previous and next to the n^{th} sleeper, respectively; the superscript *p* represents the irrecoverable component of the response; *m*, *c* and *k* correspond to the vibrating mass (kg), viscous damping coefficient (Ns/m) and elastic stiffness (N/m), respectively; *F*, *z*, $\dot{z}$ and $\ddot{z}$ are the force (N), displacement (m), velocity (m/s) and acceleration (m/s^2), respectively; c^s and k^s are the shear damping coefficient (Ns/m) and shear stiffness (N/m), respectively. The force increment $\mathrm{d}F_{\mathrm{b,n}}$ is equal to the increment in the rail seat load calculated using Equation (2) for the n^{th} sleeper whereas the force increments $\mathrm{d}F_{\mathrm{g,n}}$ and $\mathrm{d}F_{\mathrm{s,n}}$ are considered as zero. Equation (7) can be rearranged into a general force-displacement relationship form as follows:

$$d\overline{\boldsymbol{F}} = \boldsymbol{K} d\boldsymbol{z} \tag{8}$$

where $\boldsymbol{K}$ is the stiffness matrix; $d\overline{\boldsymbol{F}}$ and $d\boldsymbol{z}$ are the incremental equivalent force and displacement vectors, respectively (see APPENDIX-2). This equation can be solved using the Newmark's–β numerical integration scheme at each time instant to evaluate the complete track response.

The damping coefficients for the three substructure layers can be evaluated as follows[52]:

$$c_{\mathrm{b}} = \sqrt{\frac{E_{\mathrm{b}}\rho_{\mathrm{b}}}{(1+\nu_{\mathrm{b}})(1-\nu_{\mathrm{b}})}};\, c_{\mathrm{s}} = \sqrt{\frac{E_{\mathrm{s}}\rho_{\mathrm{s}}}{(1+\nu_{\mathrm{s}})(1-\nu_{\mathrm{s}})}};\, c_{\mathrm{g}} = \sqrt{\frac{E_{\mathrm{g}}\rho_{\mathrm{g}}}{(1+\nu_{\mathrm{g}})(1-\nu_{\mathrm{g}})}} \tag{9}$$

where the subscripts *b*, *s* and *g* denote the ballast, subballast and subgrade layers, respectively; ρ is the density (kg/m^3).

To evaluate the vibrating mass and stiffness of the substructure layers, pyramidal distribution of vertical load from the sleeper bottom to the track substructure layers is assumed, which incorporates the overlapping of the load distribution pyramids along both longitudinal (i.e., the direction of train movement) and transverse directions[36]. Figure 4 illustrates the effective region of the load distribution pyramids beneath each sleeper position. The geometry of the load distribution pyramids is first identified based on the thickness of the substructure layers, the stress distribution angles, the effective length and the width of sleeper. Subsequently, the mass of the effective region of each track layer is determined by multiplying its volume with the density. Similarly, the stiffness for each track layer is determined by using the analogy to an axially loaded bar with a variable cross-section. Complete details regarding the calculation of vibrating mass and stiffness of the substructure layers can be found elsewhere[36].

The stress distribution angle is determined by extending the approach used by Han et al.[53] to the track substructure layers:

$$\alpha = \tan^{-1}\left\{\frac{a}{h_{\mathrm{b}}}\left[\sqrt{\frac{\sigma_{\mathrm{sb}}}{\sigma_{\mathrm{bs}}}} - 1\right]\right\} \quad (10)$$

$$\beta = \tan^{-1}\left\{\frac{(a + h_{\mathrm{b}}\tan\alpha)}{h_{\mathrm{s}}}\left[\sqrt{\frac{\sigma_{\mathrm{bs}}}{\sigma_{\mathrm{sg}}}} - 1\right]\right\} \quad (11)$$

$$\gamma = \tan^{-1}\left\{\frac{(a + h_{\mathrm{b}}\tan\alpha + h_{\mathrm{s}}\tan\beta)}{h_{\mathrm{g}}}\left[\sqrt{\frac{\sigma_{\mathrm{sg}}}{\sigma_{\mathrm{go}}}} - 1\right]\right\} \quad (12)$$

where α, β and γ are the stress distribution angles (°) in ballast, subballast and subgrade, respectively; σ_{sb}, σ_{bs} and σ_{sg} are the vertical stresses (N/m^2) at the sleeper-ballast, ballast-subballast, and subballast-subgrade interfaces, respectively; h_{g} is the subgrade thickness (m); a is an equivalent radius of the sleeper-ballast contact area (m); σ_{go} is the vertical stress (N/m^2) at the bottom of the subgrade layer.

2.2.2 | Slider elements

The following sections describe the constitutive relationships used for the plastic slider elements in case of granular layers (ballast and subballast) and subgrade.

Granular layers

The constitutive relationship introduced here for the granular materials is based on the Nor-Sand model developed by Jefferies[54] and Jefferies and Shuttle[55] for triaxial and 3D loading condition, respectively. It is a state parameter based model, which has been derived from the fundamental axioms of the critical state theory. This approach allows the simulation of the response of granular materials under general stress conditions over a wide range of density and stress-states, using the same set of model parameters. The technique is based on isotropic hardening plasticity and employs an associated flow rule. The maximum dilatancy in this model is controlled by applying a limit on the hardening of the yield surface. The present relationship for the slider element employs all the parameters associated with the original Nor-Sand model with one additional parameter that characterises the behaviour under repeated loading conditions.

Yield surface. The yield surface (f) for the slider element in case of granular materials (ballast and subballast) is defined as[56]:

$$f = \frac{\eta}{M_{\mathrm{i}}} + \ln\left(\frac{p}{p_{\mathrm{i}}}\right) - 1 \tag{13}$$

where the subscript i represents the image state condition; M is the critical stress ratio; η is the stress ratio; $\eta = q/p$, where q and p are the deviatoric and mean effective stresses, respectively; $p = \boldsymbol{\sigma}_{\mathrm{kk}}/3$; $q = \sqrt{\frac{3}{2}\boldsymbol{s}_{\mathrm{ij}}\boldsymbol{s}_{\mathrm{ij}}}$, where $\boldsymbol{s}_{\mathrm{ij}}$ is the deviatoric stress tensor ($\boldsymbol{s}_{\mathrm{ij}} = \boldsymbol{\sigma}_{\mathrm{ij}} - p\delta_{\mathrm{ij}}$, where $\boldsymbol{\sigma}_{\mathrm{ij}}$ and δ_{ij} are the stress tensor and Kronecker delta, respectively). The stress state for the slider element is determined using the modified Boussinesq approach discussed in section 2.1.1. This technique of translating the boundary force into the continuum stress variables for the slider elements is consistent with the approach used by Di Prisco and Vecchiotti[57].

The image state corresponds to the condition where zero dilatancy (D) exists (i.e., $D = d\varepsilon_{\mathrm{v}}/d\varepsilon_{\mathrm{q}} = 0$, where $d\varepsilon_{\mathrm{v}}$ and $d\varepsilon_{\mathrm{q}}$ are the volumetric and deviatoric strain increments, respectively). The image mean effective stress (p_{i}) controls the size of the yield surface. The critical stress ratio corresponding to the image state is calculated as[56]:

$$M_{\mathrm{i}} = M\left[1 - \frac{N_{\mathrm{v}}\chi_{\mathrm{i}}|\Psi_{\mathrm{i}}|}{M_{\mathrm{tc}}}\right] \tag{14}$$

where the subscripts i and tc represent the image state and triaxial compression condition, respectively; N_{v} is the volumetric coupling coefficient suggested by Nova[58]; ψ_{i} is the image state parameter [$\psi_{\mathrm{i}} = \psi + \lambda \ln(p_{\mathrm{i}}/p)$]; ψ is the state parameter ($\psi = e - e_{\mathrm{c}}$); e is the current void ratio; e_c is the void ratio on the critical state line at the current mean effective stress ($e_c = \Gamma - \lambda \ln p$); Γ is the critical void ratio at p = 1 kPa; λ is the slope of the critical state line in e–ln p space; χ relates maximum dilatancy to the state parameter [$\chi_i = \chi_{tc}/(1-\lambda\chi_{tc}/M_{itc})$]; M_{itc} is the critical stress ratio corresponding to the image of the critical state for triaxial compression condition. The stress-dilatancy relationship for this model is given as[56]:

$$D_p = \frac{d\varepsilon_v^p}{d\varepsilon_q^p} = M_i - \eta \tag{15}$$

where D_p is the plastic dilatancy; $d\varepsilon_v^p$ and $d\varepsilon_q^p$ are the plastic volumetric and deviatoric strain increments, respectively. The plastic strain increments are determined using:

$$d\boldsymbol{\varepsilon}_{ij}^p = \Lambda_g \frac{\partial f(q, p, M_i, p_i)}{\partial \boldsymbol{\sigma}_{ij}} \tag{16}$$

where $d\boldsymbol{\varepsilon}_{ij}^p$ is the plastic strain increment; $\boldsymbol{\sigma}_{ij}$ is the stress tensor; Λ_g is a scalar expressed as:

$$\Lambda_g = \frac{\mathcal{J}(d\boldsymbol{\varepsilon}_{ij}^p)}{\partial f(q, p, M_i, p_i)/\partial \mathcal{J}(\boldsymbol{\sigma}_{ij})} = d\varepsilon_q^p \tag{17}$$

where $\mathcal{J}$ is the tensorial invariant. The displacement increment of the slider element is then calculated by multiplying the granular layer thickness with the plastic strain increment ($d\varepsilon_z^p$) in the vertical direction [determined using Equation (16)]. The plastic displacement rate of the slider element is computed by differentiating the plastic displacement in the vertical direction with respect to time. These values are used as an input in Equation (7) to determine the total track response.

Hardening rule. The hardening rule formulation follows the Nor-sand model[56], but, it has been modified in this study to realistically simulate the response of granular soil under repeated loading condition:

$$\frac{dp_i}{p_i} = \frac{H}{R_i}\frac{M_i}{M_{itc}}\left(\frac{p}{p_i}\right)^2 \left[e^{\left(\frac{-\chi_i \Psi_i}{M_{itc}}\right)} - \left(\frac{p_i}{p}\right)\right] d\varepsilon_q^p \tag{18}$$

where dp_i is the increment in mean effective stress at the image state; H is the hardening parameter. The modification from the original Nor-sand model is the introduction of the parameter R_i, that controls the magnitude of plastic strain accumulated during repeated loading condition. This parameter is calculated as:

$$R_i = e^{-\frac{1}{a_h}\left(1-\frac{p_i}{p_{ic}}\right)} \sqrt{\frac{p_i - p_{im}}{p_{ic} - p_{im}}} \tag{19}$$

where a_h is a cyclic hardening parameter that can be determined by calibration of the model against the experimental data; p_{im} is the minimum value of p_i observed; p_{ic} is a parameter that accumulates with the activation (or reactivation) of the slider element and is calculated as p_{ic} $(t+dt) = p_{ic}(t) + dp_i$ when the slider element is activated and $p_{ic}(t+dt) = p_{ic}(t)$, when the slider element is deactivated. As the number of activation-deactivation cycles of the slider element increases, p_{ic} increases and the magnitude of R_i decreases. Consequently, the magnitude of $d\varepsilon_q^p$ decreases with an increase in the number of activation-deactivation cycles. The conditions for activation and deactivation of the slider element are discussed in the next section.

Loading/unloading condition. In order to distinguish between the loading (activation) and unloading (deactivation) of the slider element during repeated loading conditions, the Kuhn-Tucker relations must be met[23,59]:

$$\Lambda_g \geq 0; f(q, p, M_i, p_i) \leq 0; \Lambda_g f(q, p, M_i, p_i) = 0 \quad (20)$$

Equation (20) suggests that for the activation or loading of the slider element, Λ_g must be greater than zero, the stresses must be admissible, and the yield condition remains satisfied. The unloading of the slider element occurs when the stresses are admissible, and the yield conditions are not satisfied. The unloading may also occur if the yield condition is satisfied, but Λ_g is zero.

Figure 5 shows an example of the generation of irrecoverable deformations during train-induced repeated loading. The dashed vertical lines in the figure correspond to the time of passage of individual wheel/axle. For each axle/wheel pass, the slider element remains inactive until the plastic loading condition [Equation (20)] is satisfied. During the active state of the slider element (represented by bold lines in deviatoric stress-time history in Figure 5), the magnitude of irrecoverable deformation increment ($d\varepsilon_q^p$) for each time instant is calculated using Equation (18). Subsequently, the cumulative plastic strain at any instant is determined as $\varepsilon_q^p(t + dt) = \varepsilon_q^p(t) + d\varepsilon_q^p$, where dt is the time step.

During the inactive state of the slider element, no irrecoverable deformation is generated ($d\varepsilon_q^p = 0$), and the magnitude of R_i is considered as 0. For the first active state of the slider element, the magnitude of R_i remains at unity since p_{ic} and p_i are equal. With an increase in the number of axle/wheel passes, the magnitude of R_i decreases since p_{ic} accumulates with the activation (or reactivation) of the slider element between consecutive wheel passes [see Equation (19)]. Since the plastic strain increment depends on the magnitude of R_i, it decreases with an increase in the number of axle/wheel passes.

Calibration of constitutive parameters for the ballast and subballast slider elements. The input parameters for the slider element for the granular layers (ballast and subballast) are obtained from the results of the cyclic loading triaxial tests conducted by Suiker et al.[60]. The ballast used in their study was crushed basalt, which is classified as uniformly graded gravel while, the subballast comprised of well-graded sand with gravel. The cyclic triaxial tests were carried out in a load-controlled mode at two different confining pressures (σ_c): 41.3 kPa and 68.9 kPa. At both the confining pressures, the amplitude of the cyclic stress ratio $(q/p)_{cyc}$ was taken as a specific fraction (n) of the static failure stress ratio $(q/p)_{stat,max}$.

Figure 6 illustrates a comparison between the experimental data and the results predicted using the constitutive relationship for the slider element for ballast. The symbols show the data obtained from the experiments and the solid lines show the predicted results. The model parameters used for the simulation are provided in Table 1. The critical state parameters Γ and λ can be derived using the data from multiple undrained and drained triaxial compression tests on loose to dense samples[55]. However, due to the lack of adequate test data, these parameters were selected upon the basis of engineering judgement. The parameters M_{tc} and N_v are derived by plotting the data from triaxial tests in the stress-dilatancy form, i.e., peak stress ratio (η_{max}) versus maximum dilatancy ($D_{p,max}$). A linear best-fit curve is then drawn through the data whose slope and intercept yields $(1 - N_v)$ and M_{tc}, respectively. The parameter χ_{tc} is derived by plotting the data from triaxial tests in the state-dilatancy form, i.e., $D_{p,max}$ versus ψ at maximum dilatancy. A linear best-fit curve, passing along the origin, is then drawn through the data whose slope yields the value of χ_{tc}[56]. The value of the hardening parameters H and a_h were selected based on engineering judgement.

It is apparent from Figures 6a and 6b that the predicted results are in good agreement with the experimental data at both the confining pressures. The model is able to simulate the rapid accumulation of strain during the initial stages of the repeated loading followed by a reduction in the rate of strain accumulation at the later stages of repeated loading. Thus, the present constitutive relationship can accurately capture the response of the ballast under repeated loading conditions.

Figure 7 shows a comparison of the experimental data with the results predicted using the constitutive relationship for the slider element for subballast. The experimental data and the predicted results are represented using symbols and solid lines, respectively. The model parameters used for the simulation are listed in Table 1. It is evident from Figures 7a and 7b that the present constitutive relationship predicts the accumulation of strain under repeated loading quite well in relation to the strain accumulation observed during the laboratory experiments. Thus, the present constitutive relationship can accurately simulate the behaviour of subballast under repeated loading conditions. The calibrated constitutive parameters for both the ballast and subballast, thus obtained, are used later in the parametric analyses.

Subgrade

The constitutive relationship for the plastic slider element in case of subgrade is based on the 3D elastoplastic model conceived by Ma et al.[61] to predict the mechanical behaviour of geomaterials under general stress conditions. The advantage of using this relationship is that it requires a limited number of parameters (seven parameters) to provide reasonably accurate predictions under 3D repeated loading conditions. This relationship builds on the Modified Cam-clay model, but in the characteristic stress space, which is formed by transforming the principal stress space using a parameter ξ[62]:

$$\hat{\sigma}_{\mathrm{j}} = \sigma_{\mathrm{ref}}\left(\frac{\sigma_{\mathrm{j}}}{\sigma_{\mathrm{ref}}}\right)^{\xi};\ j = 1,2,3 \tag{21}$$

where $\hat{\sigma}_{\mathrm{j}}$ is the characteristic stress (N/m^2); σ_{ref} is the reference stress (assumed to be 1 kPa in this study); σ_{j} is the principal stress (N/m^2); ξ is a dimensionless material parameter, which can be obtained by solving the following equation[62]:

$$\frac{(1+\sin\varphi_{\mathrm{c}})^{\xi} - (1-\sin\varphi_{\mathrm{c}})^{\xi}}{(1+\sin\varphi_{\mathrm{c}})^{\xi} + 2(1-\sin\varphi_{\mathrm{c}})^{\xi}} = \frac{(1+\sin\varphi_{\mathrm{e}})^{\xi} - (1-\sin\varphi_{\mathrm{e}})^{\xi}}{(1-\sin\varphi_{\mathrm{e}})^{\xi} + 2(1+\sin\varphi_{\mathrm{e}})^{\xi}} \tag{22}$$

where φ_{c} and φ_{e} are the critical state friction angles (°) under triaxial compression and extension tests, respectively. The model is based on the isotropic hardening plasticity and employs a non-associated flow rule.

Yield and plastic potential function. The yield function for the slider element is based on the Modified Cam-clay model in the characteristic stress space with plastic volumetric strain as a hardening parameter[63]:

$$f = \frac{(\lambda-\kappa)}{\xi(1+e_0)}\left[A\ln\left(\frac{\widehat{M}^2+\hat{\eta}^2}{\widehat{M}^2+\hat{\eta}_0^2}\right) + \ln\frac{\hat{p}}{\hat{p}_0}\right] - \int\frac{d\varepsilon_{\mathrm{v}}^{p}}{R} \tag{23}$$

where the symbol (^) represents the component in the characteristic stress space; subscript '0' refers to the initial value; λ and κ are the slope of critical state and swelling lines, respectively[64];

e is the void ratio; $\hat{\eta}$ is the stress ratio ($\hat{\eta} = \hat{q}/\hat{p}$, where $\hat{q}$ and $\hat{p}$ are the deviatoric and hydrostatic stress invariants, respectively); $\varepsilon_{\mathrm{v}}^{p}$ is the plastic volumetric strain; R is a parameter that controls the magnitude of plastic volumetric strain increment. $\widehat{M}$ is the critical stress ratio expressed as[62]:

$$\widehat{M} = 3\,\frac{(1+\sin\varphi_c)^{\xi} - (1-\sin\varphi_c)^{\xi}}{(1+\sin\varphi_c)^{\xi} + 2(1-\sin\varphi_c)^{\xi}} \tag{24}$$

Furthermore, A denotes a dimensionless constitutive parameter that describes the distance between normal compression line (NCL) and the critical state line (CSL), i.e.,

$$A = \frac{\xi(\widehat{N} - \widehat{\Gamma})}{(\lambda-\kappa)\ln 2} \tag{25}$$

where $\widehat{N}$ and $\widehat{\Gamma}$ are the void ratio of the NCL and CSL at $\hat{p}$ =1 kPa, respectively.

To simulate the accumulation of plastic strain with an increase in the number of load repetitions, the model employs the concept of sub-loading surfaces[65] with isotropic hardening. Three surfaces: transitional (f_{t}), current (f_{c}) and reference surfaces (f_{r}) are used, which are defined as follows[63]:

$$f_{\mathrm{t}} = A\ln\left(1+\frac{\hat{\eta}^2}{\widehat{M}^2}\right) + \ln\frac{\hat{p}}{\hat{p}_{\mathrm{xt}}} = 0 \tag{26}$$

$$f_{\mathrm{c}} = A\ln\left(1+\frac{\hat{\eta}^2}{\widehat{M}^2}\right) + \ln\frac{\hat{p}}{\hat{p}_{\mathrm{xc}}} = 0 \tag{27}$$

$$f_{\mathrm{r}} = \frac{(\lambda-\kappa)}{\xi(1+e_0)}\left[A\ln\left(1+\frac{\hat{\eta}_0^2}{\widehat{M}^2}\right) + \ln\frac{\hat{p}_0}{\hat{p}_{\mathrm{xr}}}\right] + \frac{\varepsilon_{\mathrm{v}}^{p}}{R} = 0 \tag{28}$$

where $\hat{p}_{\mathrm{xt}}$, $\hat{p}_{\mathrm{xc}}$ and $\hat{p}_{\mathrm{xr}}$ are the intersections of the transitional, current and reference surfaces with the $\hat{p}$ axis, respectively. The parameter R is determined using the following Equation (29):

$$R = e^{-\frac{1}{a_{\mathrm{h}}}\left(1-\frac{\hat{p}_{\mathrm{xc}}}{\hat{p}_{\mathrm{xr}}}\right)}\sqrt{\frac{\hat{p}_{\mathrm{xc}} - \hat{p}_{\mathrm{xt}}}{\hat{p}_{\mathrm{xr}} - \hat{p}_{\mathrm{xt}}}} \tag{29}$$

where a_{h} is the cyclic hardening parameter, that can be determined by calibrating the model against the experimental data.

The sub-loading surface f_{c} always passes through the current stress state during both activation and deactivation phases of the slider element. Whereas, the surface f_{r} expands because of the accumulated plastic strains according to the isotropic hardening rule and f_{t} evolves depending on the current state, i.e., activation or deactivation. Nevertheless, f_{r} and f_{t} retain geometrical similarity to the sub-loading surface f_{c}.

At the beginning of the activation phase, all the three surfaces are coincident, i.e., $\hat{p}_{\mathrm{xt}}$ = $\hat{p}_{\mathrm{xc}}$ = $\hat{p}_{\mathrm{xr}}$ and R = 1. During the active state of the slider element, the surfaces f_{c} and f_{r} expand simultaneously, whereas f_{t} retains its initial position. The plastic strain, thus generated, is calculated using the plastic potential function as follows:

$$d\boldsymbol{\varepsilon}_{\mathrm{ij}}^{p} = \Lambda_{\mathrm{s}} \frac{\partial g}{\partial \widehat{\boldsymbol{\sigma}}_{\mathrm{ij}}} \tag{30}$$

where $d\boldsymbol{\varepsilon}_{\mathrm{ij}}^{p}$ is the plastic strain increment; Λ_{s} is a scalar; $\widehat{\boldsymbol{\sigma}}_{\mathrm{ij}}$ is the characteristic stress tensor; g is the potential function defined by[61]:

$$g = \ln\left[\frac{\widehat{M}^2 + (2\xi - 1)\hat{\eta}^2}{\widehat{M}^2}\right] + \frac{(2\xi - 1)}{\xi}\ln\left(\frac{\hat{p}}{\hat{p}_{\mathrm{xg}}}\right) = 0 \tag{31}$$

where $\hat{p}_{\mathrm{xg}}$ is the intersection of the potential function with the $\hat{p}$ axis. The scalar Λ_{s} is calculated from[63]:

$$\Lambda_{\mathrm{s}} = \frac{-\left(\frac{\partial f}{\partial \hat{q}} d\hat{q} + \frac{\partial f}{\partial \hat{p}} d\hat{p}\right)}{\left(\frac{\partial g}{\partial \hat{p}}\right)\left(\frac{\partial f}{\partial \varepsilon_{\mathrm{v}}^{p}}\right)} \tag{32}$$

Substituting the value of g and Λ_{s} in Equation (30), the following relationship is obtained[63]:

$$d\boldsymbol{\varepsilon}_{\mathrm{ij}}^{p} = \frac{R(\lambda - \kappa)}{\xi(1 + e_0)}\left[\frac{\widehat{M}^2\hat{p}^2 + (1 - 2A)\hat{q}^2}{\hat{p}\left(\widehat{M}^2\hat{p}^2 + \hat{q}^2\right)} d\hat{p} + \frac{2A\hat{q}d\hat{q}}{\widehat{M}^2\hat{p}^2 + \hat{q}^2}\right]\left[\frac{3\xi\hat{p}\left(\widehat{\boldsymbol{\sigma}}_{\mathrm{ij}} - \hat{p}\delta_{\mathrm{ij}}\right)}{\widehat{M}^2\hat{p}^2 - \hat{q}^2} + \frac{\delta_{\mathrm{ij}}}{3}\right] \tag{33}$$

where δ_{ij} is the Kronecker delta; $d\hat{p}$ and $d\hat{q}$ are the hydrostatic and deviatoric stress increments in the characteristic stress space, respectively. The displacement increment of the slider element is then calculated by multiplying the subgrade thickness with the plastic strain increment ($d\varepsilon_{\mathrm{z}}^{p}$) in the vertical direction [determined using Equation (33)]. The plastic displacement rate of the slider element is computed by differentiating the plastic displacement of subgrade in the vertical direction with respect to time. These values are used as an input in Equation (7) to determine the total track response.

It can be noted that the parameter R controls the magnitude of plastic strain increment. During the first active state of the slider element, the surfaces f_{c} and f_{r} remain coincident, therefore, the value of R remains equal to 1. As soon as the slider is deactivated, the surface f_{t} expands and become coincident with f_{c}, i.e., $\hat{p}_{\mathrm{xt}}$ = $\hat{p}_{\mathrm{xc}}$ and R = 0, whereas f_{r} remains in the position acquired at the end of active state. As the deactivation phase proceeds, both f_{c} and f_{t}

shrink simultaneously (keeping $R = 0$) while f_r retains its position. Since the magnitude of R is equal to 0, no plastic strain is generated during the deactivation stage.

As the reactivation of the slider element starts, both f_c and f_r expand simultaneously while the surface f_t remains in the position acquired at the end of deactivation stage. However, the surfaces f_c and f_r are not coincident during reactivation and the value of R varies between 0 and 1. The plastic strain generated during reactivation can be calculated using Equation (33). Since the magnitude of R remains below 1 during reactivation, the magnitude of plastic strain is less than that in the first active stage. Thus, the model can simulate the reduction in the plastic strain increment with an increase in the number of load repetitions or activation-deactivation cycles of the slider element. The conditions for activation and deactivation of the slider element are discussed in the next section.

Loading/unloading condition. To distinguish between the loading (activation) and unloading (deactivation) of the slider element during repeated loading conditions, the Kuhn-Tucker relations must be met[23,59]:

$$\Lambda_\mathrm{s} \geq 0; f(\hat{q}, \hat{p}, \varepsilon_\mathrm{v}^p) \leq 0; \Lambda_\mathrm{s} f(\hat{q}, \hat{p}, \varepsilon_\mathrm{v}^p) = 0 \quad (34)$$

Equation (34) indicates that for the activation or loading of the slider element for the subgrade, Λ_s must be greater than zero, the stresses must be admissible, and the yield criterion remains satisfied. The unloading of the slider element occurs when the stresses are admissible, and the yield conditions are not satisfied. The unloading may also occur if the yield condition is satisfied, but Λ_s is zero.

Calibration of parameters for the subgrade slider element. In this study, the model parameters for the subgrade slider element are obtained from the results of the laboratory cyclic triaxial tests conducted by Wichtmann[66]. In Figure 8, the predicted results are compared with the data obtained from the laboratory cyclic triaxial tests. Table 2 provides the details of the input parameters used for the simulation. The parameters λ and κ are derived using the data from multiple isotropic compression and swelling tests on soil specimens. The parameter φ_c is the critical state friction angle under triaxial compression. The value of ξ and parameter A are determined using Equations (22) and (25), respectively. The hardening parameter a_h is derived by calibrating the model against the experimental data.

Referring to Figure 8a, it can be observed that the predicted stress-strain behaviour is in an acceptable agreement with the experimental results at a deviatoric stress amplitude (q^{ampl})

and mean stress (p^{av}) of 80 kPa and 200 kPa, respectively. The irrecoverable component of the axial strain in each load cycle is high during the initial stages of loading and then decreases with an increase in the number of load cycles. In Figure 8b, the variation of accumulated axial strain with the number of load cycles predicted using the present constitutive relationship is compared with the experimental results, at different deviatoric stress amplitude (q^{ampl}). It can be observed that the predicted results are in an acceptable agreement with the laboratory data. The predicted results vary by 1-15% from the experimental results at 10,000 load cycles. The accuracy of the predictions can be increased further by using more advanced calibration procedure[23,67].

It can be noted that the accumulated axial strain increases rapidly during the initial phase, followed by a reduction in the rate of axial strain accumulation. The predicted results can also capture the increase in the magnitude of accumulated axial strain with an increase in the deviatoric stress amplitude. Thus, it is evident that the present approach can accurately capture the response of the soil under repeated loading conditions.

3 | MODEL VALIDATION

The dynamic equilibrium equation [Equation (7)] is solved using the Newmark's–β numerical integration scheme at each time instant. The solution of the equation yields the variation of total displacement, velocity and acceleration of the three substructure layers with time. Figure 9 presents the flowchart used to evaluate the total viscoelasto-plastic response of the substructure layers subjected to the repeated traffic loadings. The input data required in the analysis include the train properties; track properties, such as sleeper spacing, density, Young's modulus, Poisson's ratio, shear stiffness, shear damping and thickness of the substructure layers; and the constitutive parameters for the slider elements. Once the input parameters are derived, the effective region of the substructure layers below each sleeper is identified, and the vibrating mass, damping coefficient and stiffness of the track layers are calculated. Subsequently, the rail seat load-time history is derived at each sleeper location. For the slider elements, the continuum stress type parameters (such as p, q) are required as input for the constitutive model. Therefore, the stress distribution in the track layers is estimated for each time instant using the method described in Section 2.1.1. If the stress state in a substructure layer at any instant reaches the yield surface (and the plastic loading conditions are satisfied), the irrecoverable strain is calculated using the constitutive relationship of the slider element. Since the method is an implicit step-by-step approach, the plastic strain is evaluated at each time instant. Once the irrecoverable strain is calculated, it is multiplied by the thickness of the individual layer to yield the plastic displacement. The plastic velocity is then calculated by differentiating the plastic displacement with respect to time. Finally, the total track response is evaluated by solving the dynamic equilibrium equation [Equation (7)] at each time instant. The analysis is continued till the desired number of wheels/axles have passed the sleeper location (i.e., when the time elapsed, $t = t_f$, where t_f is the final time for analysis). It must be noted that the track response in the present method is evaluated at individual sleeper locations. The deformation profile of the track between the sleeper locations can be determined by means of an interpolation technique.

To validate the reliability of the model, the results calculated using the present approach are compared with the in-situ measurements reported by Gräbe et al.[68], Gräbe and Shaw[69] and Priest et al.[13]. Gräbe et al.[68] reported the vertical deformation and the stress distribution in the substructure layers in a heavy haul track in South Africa. The track comprised of a 300 mm thick ballast layer overlying the formation, which constitutes of four 200 mm thick layers of engineered fill (Layer 2) and the natural ground (comprising of weathered tillite). Table 3 lists the input parameters used in the model predictions. Figure 10a illustrates the variation of vertical stress with time at different depth below the formation level (i.e., below the ballast-engineered fill interface) during the passage of a coal wagon. It is evident that the predicted results are in good agreement with the in-situ measurements. The model over predicts the vertical stress at the formation level (0 mm). However, the stress distribution with depth is the same as that observed in the field. At the formation level (0 mm), multiple peaks are visible, which correspond to the passage of individual axles. However, the influence of individual axles diminishes with depth.

The variation of transient (or resilient) deformation with depth in the formation (engineered fill) layer computed using the present approach is compared with the in-situ measurements recorded by Gräbe et al.[68] in Figure 10b. It can be seen that the predicted results are in an acceptable agreement with the in-situ measurements. The deformation decreases with an increase in depth from the ballast-engineered fill interface.

The variation of resilient vertical sleeper displacement with time during the passage of a 26-tonne axle load coal wagon predicted using the present approach is compared with the in-situ measurements recorded by Priest et al.[13] in Figure 11a. Table 3 lists the input parameters used in the model predictions. It is evident that the predicted results are in reasonable agreement with the field data. Figure 11b shows the increase in vertical and horizontal stresses at a depth of 800 mm beneath the sleeper bottom, predicted using the present approach and that using FE analysis by Priest et al.[13]. It can be observed that the results predicted using the present technique are in good agreement with the data reported by Priest et al.[13].

The accumulation of irrecoverable deformation with tonnage (in million gross tonnes, MGT) predicted using the present technique is compared with the in-situ measurements reported by Gräbe and Shaw[69] in Figure 12. Tables 1, 2 and 3 list the input parameters used in the model predictions. It can be seen that the predicted results are in reasonable agreement with the field data. An overestimation of the cumulative deformation in the initial stages of loading may be attributed to the fact that the present method predicts a high rate of settlement during the initial loading stage followed by a reduction in the settlement rate with an increase in tonnage. However, the rate of settlement in the field measurements fluctuates due to the uncertainties associated with the train loading and temporal variation in the subgrade properties due to seasonal fluctuations in the temperature, as mentioned by Gräbe and Shaw[69]. Nevertheless, the magnitude of predicted cumulative deformation is similar to the in-situ measurements when the track is subjected to a tonnage of about 350 MGT (which may be more commonly associated with track deterioration in comparison to initial stages of loading). Therefore, the present approach can accurately capture the irrecoverable response of the rail track substructure layers over a period of time.

Thus, the present technique can accurately predict the transient, and irrecoverable track response under the train traffic-induced repeated loads. The constitutive parameters for the slider elements can be calculated using the data from laboratory triaxial tests (both static and cyclic) on track materials (preferably under true triaxial conditions). The proposed approach is simple, computationally efficient and can predict the long-term performance of the ballasted railway tracks. This method can also serve as a tool for practising engineers to optimise the track performance.

However, the present method neglects the shear stress reversal or the principal stress rotation that the substructure experiences when a moving load is passing at a specific location. The principal stress rotation can significantly influence the permanent deformation behaviour of the geomaterials. The future investigations shall deal with this limitation to further enhance the accuracy of the proposed method.

4 | RESULTS AND DISCUSSION

A parametric analysis is carried out to investigate the influence of axle load (Q_a), train speed (V) and thickness of granular layers (h_{gl}) on the stress distribution and cumulative track settlement. The values of the parameters used in the analysis are listed in Table 3. The model parameters that were previously calibrated using the experimental data reported by Suiker et al.[60] and Wichtmann[66] are used for the slider element for granular layers and subgrade, respectively (see Tables 1 and 2). The results are calculated for the passage of a train consisting of 32 axles, with an axle configuration similar to the Acela express train. In each analysis, only one parameter is varied at a time while nominal values are assigned to other parameters. The nominal value of the axle load is 25 t while the nominal values of ballast and subballast thicknesses are provided within the parenthesis in Table 3.

4.1 | Influence of axle load

The magnitude of axle load is varied between 20 t and 30 t to study its influence on the response of the railway track. The train speed for this analysis is considered as 150 km/h. Figure 13 shows the variation of vertical stress (σ_v) distribution with depth (z) calculated using the present method at three different axle loads. It can be observed that the vertical stress decreases with an increase in depth. For each case, the traffic-induced vertical stress at the subgrade top is about 36% of that at the ballast top. This finding highlights the critical function served by the granular layers, i.e., to reduce the magnitude of traffic-induced stresses transferred to the subgrade soil to a safe level[1]. It can also be noted that the peaks in the vertical stress versus time plots corresponding to the passage of individual axles are visible at the ballast top (0 mm). However, the effect of individual axle diminishes with depth. This finding is similar to that observed in the 3D FE analyses conducted by Powrie et al.[70]. As the axle load increases, the traffic-induced vertical stress in the three substructure layers increases. Interestingly, the effect of axle load increment is visible only in the top portion of the subgrade soil, and this effect diminishes with depth. At a depth of 3000 mm, there is an insignificant change in the vertical stress with an increase in axle load.

Figure 14 shows the distribution of accumulated settlement with depth after a cumulative tonnage of 20 million gross tonnes (MGT) for three different axle loads. It is evident that the settlement increases with an increase in the axle load. The overall track settlement increases by 41% with an increase in axle load from 20 t to 25 t. The increment rises to 73% when the axle load increases from 25 t to 30 t. The settlement of the granular layers (s_{gl}) also increases from 3.6 mm to 5.9 mm with an increase in axle load from 20 t to 30 t, respectively. Thus, it is apparent that an increase in the axle load may significantly increase the cumulative deformation in the existing tracks, resulting in a degradation of track geometry.

4.2 | Influence of train speed

The train speed is varied between 100 km/h and 200 km/h to investigate its influence on the magnitude of cumulative deformation in the track layers. Figure 15 shows the distribution of settlement with depth after a cumulative tonnage of 25 MGT at three different train speeds. It can be observed that the magnitude of settlement accumulated in the track increases with an increase in train speed. The overall track settlement increases by 19% as the train speed increases from 100 km/h to 150 km/h. The increment rises to 26% when the train speed increases from 150 km/h to 200 km/h.

It must be noted that the effect of train speed in this study is considered by employing a dynamic amplification factor (DAF), which is a multiplier to the axle (or wheel) load. This DAF increases with an increase in train speed, and consequently, the magnitude of stress and deformation accumulated in the track increases with train speed. The DAF accounts for the increment in track response due to various effects such as the dynamic vehicle-track interaction[24,39,71], the relative velocity of the vehicle with respect to the critical wave propagation velocity of the track-ground system[37,38,71-74] and the sleeper passing frequency[7,26,38,73].

In this study, the DAF is calculated using the empirical expression proposed by Nimbalkar and Indraratna[5]:

$$DAF = 1 + i_1 \left(\frac{V}{D_\mathrm{w}} \right)^{i_2} \tag{35}$$

where i_1 and i_2 are the empirical parameters whose values range between 0.0052-0.0065 and between 0.75-1.02, respectively, depending on the axle load and subgrade type; V and D_w are the train speed (km/h) and diameter of train wheel (m), respectively. This expression was developed using the field data, and it considers the influence of the subgrade properties (which affects the natural frequency and critical wave propagation velocity of the track-ground system) on the load amplification.

The present study essentially captures the increment in track response due to the effects discussed above with minor contribution from the dynamic vehicle-track interaction as the track is assumed to be straight and free from inhomogeneities.

4.3 | Influence of granular layer thickness

The granular layer thickness, or the combined thickness of ballast and subballast layers, is a crucial parameter that influences the overall track stiffness and stress transfer. In this study, the thickness of the granular layer is varied between 0.45 m and 0.9 m using two approaches. In the first approach, the ballast thickness is assigned a nominal value, and the subballast thickness is varied. Whereas, in the second approach, the subballast thickness is kept constant while the ballast thickness is varied. The train speed for this analysis is considered as 100 km/h.

Figure 16 shows the variation of settlement accumulated in the subgrade layer (s_g) with tonnage at different granular layer thicknesses. It can be observed that the subgrade settlement decreases with an increase in the granular layer thickness. The subgrade settlement decreases by almost 56% with an increase in granular layer thickness from 0.45 to 0.9 m. This reduction in the settlement is due to a decrease in subgrade stress owing to an increase in the distance between subgrade top and sleeper bottom, and higher stress spreading ability of the thicker granular layers[2].

Figure 17 shows the variation of settlement accumulated in the track substructure layers with granular layer thickness, after a cumulative tonnage of 25 MGT. It can be observed from Figure 17a that the subgrade settlement decreases rapidly with an increase in granular layer thickness from 0.45 to 0.7 m (13.3 mm). However, the magnitude of settlement reduction decreases as the granular layer thickness increases further (a reduction of 3 mm with an increase in the granular layer thickness from 0.7 to 0.9 m). It can be noted that the subgrade settlement is almost identical for both the approaches used in this study. This observation is ascribed to similar stress distribution in the subgrade layer for the two approaches, which is a consequence of a large difference between Young's modulus of subgrade and granular layers, used in this study. Referring to Figure 17b, it can be observed that the settlement in the granular layers increases with an increase in granular layer thickness. The increment is higher for the case when the subballast thickness is increased and the ballast thickness is kept constant. However, this difference is negligible in comparison with the total track settlement.

5 | CONCLUSIONS

In this study, a new rheological approach, combining plastic slider, elastic springs and viscous dampers, is developed to predict the transient and long-term response of the track substructure layers under train traffic-induced repeated loading. The novel feature of the proposed approach is the use of plastic slider elements to capture the irrecoverable response of the substructure layers. Another feature is the consideration of three substructure layers, which is a more appropriate technique as compared to the existing methods that simplify the track substructure as single or double-layered. To validate the methodology, the predicted results have been compared with the in-situ measurements reported in the literature. A good agreement between the predicted results and the field data has verified the accuracy of the model. The parametric investigation highlights the significant influence of axle load, train speed and granular layer thickness, on the accumulated settlement in the track layers. An increment in the total thickness of granular layers significantly reduces the cumulative settlement in the subgrade layer. The proposed methodology is simple yet comprehensive and can be used to predict the design life of the track. It may also assist the practising engineers to plan the maintenance and rehabilitation of the existing railway tracks.

ACKNOWLEDGEMENT

The first author gratefully acknowledges the support rendered by an Australian government research training program (ARTP) fellowship. The authors thank the anonymous reviewer for providing valuable comments and suggestions.

DATA AVAILABILITY STATEMENT

Some or all data, models, or code that support the findings of the study are available from the corresponding author upon reasonable request.

ORCID

Piyush Punetha https://orcid.org/0000-0002-0812-4708
Sanjay Nimbalkar https://orcid.org/0000-0002-1538-3396
Hadi Khabbaz https://orcid.org/0000-0001-6637-4601

REFERENCES

1. Selig ET, Waters JM. *Track geotechnology and substructure management.* London: Thomas Telford; 1994.
2. Li D, Selig ET. Method for railroad track foundation design. I: Development. *J Geotech Eng.* 1998;124(4):316-322. https://doi.org/10.1061/(asce)1090-0241(1998)124:4(316)
3. Heath DL, Shenton MJ, Sparrow RW, Waters JM. Design of conventional rail track foundations. *Proc Inst Civ Engrg.* 1972;51:251-267.
4. Li D, Hyslip J, Sussmann T, Chrismer S. *Railway geotechnics.* Boca Raton, USA: Taylor and Francis; 2016.
5. Nimbalkar S, Indraratna B. Improved performance of ballasted rail track using geosynthetics and rubber shockmat. *J Geotech Geoenviron Eng.* 2016;142(8). https://doi.org/10.1061/(asce)gt.1943-5606.0001491

6. Bian X, Jiang H, Chen Y. Accumulative deformation in railway track induced by high-speed traffic loading of the trains. *Earthq Eng Eng Vib.* 2010;9(3):319-326. https://doi.org/10.1007/s11803-010-0016-2
7. Esveld C. *Modern railway track.* Delft, The Netherlands: MRT-Productions; 2001.
8. Nielsen JCO, Li X. Railway track geometry degradation due to differential settlement of ballast/subgrade – Numerical prediction by an iterative procedure. *J Sound Vib.* 2018;412:441-456. https://doi.org/10.1016/j.jsv.2017.10.005
9. Indraratna B, Nimbalkar S. Stress-strain degradation response of railway ballast stabilized with geosynthetics *J Geotech Geoenviron Eng.* 2013;139(5):684-700. https://doi.org/10.1061/(asce)gt.1943-5606.0000758
10. Dahlberg T. Some railroad settlement models–a critical review. *Proc Inst Mech Eng F J Rail Rapid Transit.* 2001;215(4):289-300. https://doi.org/10.1243/0954409011531585
11. Lekarp F, Isacsson U, Dawson A. State of the art. II: Permanent strain response of unbound aggregates. *J Transp Eng.* 2000;126(1):76-83. https://doi.org/10.1061/(asce)0733-947x(2000)126:1(76)
12. Li L, Nimbalkar S, Zhong R. Finite element model of ballasted railway with infinite boundaries considering effects of moving train loads and Rayleigh waves. *Soil Dyn Earthquake Eng.* 2018;114:147-153. https://doi.org/10.1016/j.soildyn.2018.06.033
13. Priest JA, Powrie W, Yang L, Grabe PJ, Clayton CRI. Measurements of transient ground movements below a ballasted railway line. *Géotechnique.* 2010;60(9):667-677. https://doi.org/10.1680/geot.7.00172
14. Yang LA, Powrie W, Priest JA. Dynamic stress analysis of a ballasted railway track bed during train passage. *J Geotech Geoenviron Eng.* 2009;135(5):680-689. https://doi.org/10.1061/(ASCE)GT.1943-5606.0000032
15. Yang YB, Hung HH. A 2.5D finite/infinite element approach for modelling visco-elastic bodies subjected to moving loads. *Int J Numer Methods Eng.* 2001;51(11):1317-1336. https://doi.org/10.1002/nme.208
16. Kuo CM, Huang CH. Two approaches of finite-element modeling of ballasted railway track. *J Geotech Geoenviron Eng.* 2009;135(3):455-458. https://doi.org/10.1061/(ASCE)1090-0241(2009)135:3(455)
17. Banimahd M, Woodward P, Kennedy J, Medero G. Three-dimensional modelling of high speed ballasted railway tracks. *Proc Inst Civ Eng Transp.* 2013;166(2):113-123. https://doi.org/10.1680/tran.9.00048
18. Galvín P, Mendoza D, Connolly D, Degrande G, Lombaert G, Romero A. Scoping assessment of free-field vibrations due to railway traffic. *Soil Dyn Earthquake Eng.* 2018;114:598–614. https://doi.org/10.1016/j.soildyn.2018.07.046
19. Li X, Ekh M, Nielsen JCO. Three-dimensional modelling of differential railway track settlement using a cycle domain constitutive model. *Int J Numer Anal Methods Geomech.* 2016;40(12):1758-1770. https://doi.org/10.1002/nag.2515
20. Wang H, Markine V. Modelling of the long-term behaviour of transition zones: Prediction of track settlement. *Eng Struct.* 2018;156:294-304. https://doi.org/10.1016/j.engstruct.2017.11.038
21. Varandas JN, Paixão A, Fortunato E, Zuada Coelho B, Hölscher P. Long-term deformation of railway tracks considering train-track interaction and non-linear resilient behaviour of aggregates – a 3D FEM implementation. *Comput Geotech.* 2020;126:103712.
22. Varandas JN, Hölscher P, Silva MAG. Settlement of ballasted track under traffic loading: Application to transition zones. *Proc Inst Mech Eng F J Rail Rapid Transit.* 2013;228(3):242-259. https://doi.org/10.1177/0954409712471610

23. Suiker ASJ, De Borst R. A numerical model for the cyclic deterioration of railway tracks. *Int J Numer Methods Eng.* 2003;57(4):441-470. http://dx.doi.org/10.1002/nme.683
24. Knothe KL, Grassie SL. Modelling of railway track and vehicle/track interaction at high frequencies. *Veh Syst Dyn.* 1993;22(3-4):209-262. https://doi.org/10.1080/00423119308969027
25. Connolly DP, Kouroussis G, Laghrouche O, Ho CL, Forde MC. Benchmarking railway vibrations – Track, vehicle, ground and building effects. *Constr Build Mater.* 2015;92:64-81. https://doi.org/10.1016/j.conbuildmat.2014.07.042
26. Metrikine AV, Popp K. Vibration of a periodically supported beam on an elastic half-space. *Eur J Mech A Solids.* 1999;18(4):679-701. https://doi.org/10.1016/s0997-7538(99)00141-2
27. Hunt HE. Settlement of railway track near bridge abutments. *Proc Inst Civ Eng Transport.* 1997;123(1).
28. Basu D, Kameswara Rao NSV. Analytical solutions for Euler-Bernoulli beam on visco-elastic foundation subjected to moving load. *Int J Numer Anal Methods Geomech.* 2013;37(8):945-960. https://doi.org/10.1002/nag.1135
29. Dieterman H, Metrikine V. Steady-state displacements of a beam on an elastic half-space due to a uniformly moving constant load. *Eur J Mech A Solids.* 1997;16(2):295-306.
30. Kaynia AM, Madshus C, Zackrisson P. Ground vibration from high-speed trains: Prediction and countermeasure. *J Geotech Geoenviron Eng.* 2000;126(6):531-537. https://doi.org/10.1061/(asce)1090-0241(2000)126:6(531)
31. Takemiya H, Bian X. Substructure simulation of inhomogeneous track and layered ground dynamic interaction under train passage. *J Eng Mech.* 2005;131(7):699-711. https://doi.org/10.1061/(ASCE)0733-9399(2005)131:7(699)
32. Sheng X, Jones CJC, Petyt M. Ground vibration generated by a harmonic load acting on a railway track. *J Sound Vib.* 1999;225(1):3-28. https://doi.org/10.1006/jsvi.1999.2232
33. Sun YQ, Dhanasekar M. A dynamic model for the vertical interaction of the rail track and wagon system. *Int J Solids Struct.* 2002;39(5):1337-1359. https://doi.org/10.1016/s0020-7683(01)00224-4
34. Zhai WM, Wang KY, Lin JH. Modelling and experiment of railway ballast vibrations. *J Sound Vib.* 2004;270(4-5):673-683. https://doi.org/10.1016/s0022-460x(03)00186-x
35. Choudhury D, Bharti RK, Chauhan S, Indraratna B. Response of multilayer foundation system beneath railway track under cyclic loading. *J Geotech Geoenviron Eng.* 2008;134(10):1558-1563. https://doi.org/10.1061/(ASCE)1090-0241(2008)134:10(1558)
36. Punetha P, Nimbalkar S, Khabbaz H. Analytical evaluation of ballasted track substructure response under repeated train loads. *Int J Geomech.* 2020;20(7):04020093. https://doi.org/10.1061/(ASCE)GM.1943-5622.0001729
37. Suiker ASJ, Metrikine AV, De Borst R. Dynamic Behaviour of a Layer of Discrete Particles, Part 1: Analysis of Body Waves and Eigenmodes. *Journal of Sound and Vibration.* 2001;240(1):1-18. https://doi.org/10.1006/jsvi.2000.3202
38. Suiker ASJ, Metrikine AV, De Borst R. Dynamic Behaviour of a Layer of Discrete Particles, Part 2: Response to a Uniformly Moving, Harmonically Vibrating Load. *Journal of Sound and Vibration.* 2001;240(1):19-39. https://doi.org/10.1006/jsvi.2000.3203
39. Doyle NF. Railway track design a review of current practice. In: Economics BoT, ed. Canberra: Australian government publishing service; 1980.

40. AS 1085.14. Railway track material, Part 14: Prestressed concrete sleepers. In: Australian Standards; 2019.
41. Selig ET, Li D. Track modulus: Its meaning and factors influencing it. *Transp Res Rec.* 1994;1470:47-54.
42. Le Pen L, Milne D, Thompson D, Powrie W. Evaluating railway track support stiffness from trackside measurements in the absence of wheel load data. *Canadian Geotechnical Journal.* 2016;53(7):1156-1166. https://doi.org/10.1139/cgj-2015-0268
43. Mishra D, Boler H, Tutumluer E, Hou W, Hyslip JP. Deformation and Dynamic Load Amplification Trends at Railroad Bridge Approaches. *Transp Res Rec.* 2017;2607(1):43-53. https://doi.org/10.3141/2607-07
44. Mishra D, Tutumluer E, Boler H, Hyslip J, Sussmann T. Railroad track transitions with multidepth deflectometers and strain gauges. *Transp Res Rec.* 2014;2448(1):105–114. https://doi.org/10.3141/2448-13
45. Waterways Experiment Station. *Investigations of pressures and deflections for flexible pavements: Report no. 4: Homogeneous sand test section.* Vicksburg, Mississippi1954. 3-323.
46. Ahlvin R, Ulery H. Tabulated values for determining the complete pattern of stresses, strains, and deflections beneath a uniform circular load on a homogeneous half space. *Highway Research Board Bulletin.* 1962;342.
47. Poulos H, Davis E. *Elastic solutions for soil and rock mechanics.* John Wiley & Sons; 1974.
48. Palmer L, Barber E. Soil displacement under a circular loaded area. *Highway Research Board Bulletin.* 1940;20:279-286.
49. Odemark N. Investigations as to the elastic properties of soils and design of pavements according to the theory of elasticity. *Statens Vaginstitut, Meddelande* 1949;77.
50. Hirai H. Settlements and stresses of multi-layered grounds and improved grounds by equivalent elastic method. *Int J Numer Anal Methods Geomech.* 2008;32(5):523-557. https://doi.org/10.1002/nag.636
51. Nimbalkar S, Punetha P, Kaewunruen S. Performance improvement of ballasted railway tracks using geocells: present state of the art. In: Sitharam TG, Hegde A, Kolathayar S, eds. *Geocells. Springer Transactions in Civil and Environmental Engineering.* Springer; 2020. https://doi.org/10.1007/978-981-15-6095-8_11
52. Nimbalkar S, Indraratna B, Dash SK, Christie D. Improved performance of railway ballast under impact loads using shock mats. *J Geotech Geoenviron Eng.* 2012;138(3):281-294. https://doi.org/10.1061/(asce)gt.1943-5606.0000598
53. Han J, Pokharel SK, Yang X, et al. Performance of Geocell-Reinforced RAP Bases over Weak Subgrade under Full-Scale Moving Wheel Loads. *J Mater Civ Eng.* 2011;23(11):1525-1534. https://doi.org/10.1061/(asce)mt.1943-5533.0000286
54. Jefferies MG. Nor-Sand: a simple critical state model for sand. *Géotechnique.* 1993;43(1):91-103. https://doi.org/10.1016/0148-9062(93)92281-t
55. Jefferies MG, Shuttle DA. Dilatancy in general Cambridge-type models. *Géotechnique.* 2002;52(9):625–638. https://doi.org/10.1680/geot.2002.52.9.625
56. Jefferies MG, Been K. *Soil liquefaction: a critical state approach.* Boca Raton, FL: CRC press; 2015.
57. Di Prisco C, Vecchiotti M. A rheological model for the description of boulder impacts on granular strata. *Geotechnique.* 2006;56(7):469–482.
58. Nova R. A constitutive model for soil under monotonic and cyclic loading. In Soil mechanics transient and cyclic loads. In: Pande GN, Zienkiewicz OC, eds. *Soil mechanics transient and cyclic loads* Chichester: Wiley; 1982:343-373.
59. Simo JC, Hughes TJR. *Computational Inelasticity.* Vol 7. New York: Springer; 1998.

60. Suiker ASJ, Selig ET, Frenkel R. Static and cyclic triaxial testing of ballast and subballast. *J Geotech Geoenviron Eng.* 2005;131(6):771-782. https://doi.org/10.1061/(ASCE)1090-0241(2005)131:6(771)
61. Ma C, Lu D, Du X, Zhou A. Developing a 3D elastoplastic constitutive model for soils: A new approach based on characteristic stress. *Comput Geotech.* 2017;86:129-140. https://doi.org/10.1016/j.compgeo.2017.01.003
62. Lu D, Ma C, Du X, Jin L, Gong Q. Development of a new nonlinear unified strength theory for geomaterials based on the characteristic stress concept. *Int J Geomech.* 2017;17(2). https://doi.org/10.1061/(asce)gm.1943-5622.0000729
63. Lu D, Li X, Du X, Liang J. A simple 3D elastoplastic constitutive model for soils based on the characteristic stress. *Comput Geotech.* 2019;109:229-247. https://doi.org/10.1016/j.compgeo.2019.02.001
64. Roscoe K, Burland J. On the generalized stress-strain behaviour of wet clay. In: Heyman J, Leckie F, eds. *Engineering plasticity*. Cambridge: Cambridge University Press; 1968:535–609.
65. Hashiguchi K. Subloading surface model in unconventional plasticity. *Int J Solids Struct.* 1989;25(8):917-945. https://doi.org/10.1016/0020-7683(89)90038-3
66. Wichtmann T. *Explicit accumulation model for non-cohesive soils under cyclic loading*. Germany, Ruhr-Universität Bochum; 2005.
67. Luenberger DG. *Introduction to linear and nonlinear programming.* Reading, MA: Addison-wesle; 1973.
68. Gräbe P, Clayton C, Shaw F. Deformation measurement on a heavy haul track formation. 8th International Heavy Haul Conference; 2005; Rio de Janeiro, Brazil.
69. Gräbe P, Shaw F. Design life prediction of a heavy haul track foundation. *Proc Inst Mech Eng F Rail Rapid Transit* 2010;224(5):337–344. https://doi.org/10.1243/09544097jrrt371
70. Powrie W, Yang LA, Clayton CRI. Stress changes in the ground below ballasted railway track during train passage. *Proc Inst Mech Eng F J Rail Rapid Transit* 2007;221(F2):247-262. https://doi.org/10.1243/0954409jrrt95
71. Metrikine AV, Verichev SN. Instability of vibrations of a moving two-mass oscillator on a flexibly supported Timoshenko beam. *Archive of Applied Mechanics.* 2001;71:613-624
72. Dieterman HA, Metrikine AV. The equivalent stiffness of a half space interacting with a beam. Critical velocities of a moving load along the beam. *European Journal of Mechanics and Solids.* 1996;15(1):67-90.
73. Vostroukhov AV, Metrikine AV. Periodically supported beam on a visco-elastic layer as a model for dynamic analysis of a high-speed railway track. *Int J Solids Struct.* 2003;40(21):5723-5752. https://doi.org/10.1016/s0020-7683(03)00311-1
74. Suiker ASJ, de Borst, R., Esveld C. Critical behaviour of a Timoshenko beam-half plane system under a moving load. *Archive of Applied Mechanics.* 1998;68:158-168.
75. Oscarsson J, Dahlberg T. Dynamic train/track/ballast interaction - computer models and full-scale experiments. *Veh Syst Dyn.* 1998;29(S1):73-84. https://doi.org/10.1080/00423119808969553

APPENDIX-1

VERTICAL LOAD TRANSFER FROM SUPERSTRUCTURE TO SUBSTRUCTURE

Figure A1 illustrates the transfer of train-induced loading from the superstructure to the substructure layers of the track. The vertical wheel load (Q) is transmitted from the rails to multiple sleepers via the rail seats. This load is termed as the rail seat load (Q_{r}). In the present approach, the rail seat load is applied to the ballast surface over a circular sleeper-ballast contact area, whose size depends on the sleeper dimensions. The sleeper-ballast contact pressure (σ_{sb}) is considered to be uniformly distributed and is calculated by dividing the rail seat load with the sleeper-ballast contact area. The stress distribution in the track substructure layers is then calculated using the Boussinesq solutions (after transforming multiple substructure layers into a single layer) for a uniformly loaded circular footing.

APPENDIX-2

The incremental equivalent force vector is determined as:

$$\begin{aligned} d\overline{\boldsymbol{F}} = {} & d\boldsymbol{F} - \boldsymbol{M}d\ddot{\boldsymbol{z}} - \boldsymbol{C}d\dot{\boldsymbol{z}} - \boldsymbol{C}^{\boldsymbol{p}}d\dot{\boldsymbol{z}}^{\boldsymbol{p}} - \boldsymbol{K}^{\boldsymbol{p}}d\boldsymbol{z}^{\boldsymbol{p}} + \boldsymbol{C}'\{d\dot{\boldsymbol{z}}_{\mathbf{n+1}} + d\dot{\boldsymbol{z}}_{\mathbf{n-1}}\} + \boldsymbol{K}'\{d\boldsymbol{z}_{\mathbf{n+1}} + d\boldsymbol{z}_{\mathbf{n-1}}\} \\ & - \boldsymbol{C}^{\boldsymbol{p}'}\{d\dot{\boldsymbol{z}}^{\boldsymbol{p}}_{\mathbf{n+1}} + d\dot{\boldsymbol{z}}^{\boldsymbol{p}}_{\mathbf{n-1}}\} - \boldsymbol{K}^{\boldsymbol{p}'}\{d\boldsymbol{z}^{\boldsymbol{p}}_{\mathbf{n+1}} + d\boldsymbol{z}^{\boldsymbol{p}}_{\mathbf{n-1}}\} \end{aligned} \tag{36}$$

where, $$d\mathbf{z} = \begin{Bmatrix} dz_{\mathrm{g,n}} \\ dz_{\mathrm{s,n}} \\ dz_{\mathrm{b,n}} \end{Bmatrix};\ d\dot{\boldsymbol{z}} = \begin{Bmatrix} d\dot{z}_{\mathrm{g,n}} \\ d\dot{z}_{\mathrm{s,n}} \\ d\dot{z}_{\mathrm{b,n}} \end{Bmatrix};\ d\ddot{\boldsymbol{z}} = \begin{Bmatrix} d\ddot{z}_{\mathrm{g,n}} \\ d\ddot{z}_{\mathrm{s,n}} \\ d\ddot{z}_{\mathrm{b,n}} \end{Bmatrix};\ d\boldsymbol{z}^{\boldsymbol{p}} = \begin{Bmatrix} dz^{p}_{\mathrm{g,n}} \\ dz^{p}_{\mathrm{s,n}} \\ dz^{p}_{\mathrm{b,n}} \end{Bmatrix};\ d\dot{\boldsymbol{z}}^{\boldsymbol{p}} = \begin{Bmatrix} d\dot{z}^{p}_{\mathrm{g,n}} \\ d\dot{z}^{p}_{\mathrm{s,n}} \\ d\dot{z}^{p}_{\mathrm{b,n}} \end{Bmatrix} \tag{37}$$

$$d\dot{\boldsymbol{z}}_{\mathbf{n+1}} = \begin{Bmatrix} d\dot{z}_{\mathrm{g,n+1}} \\ d\dot{z}_{\mathrm{s,n+1}} \\ d\dot{z}_{\mathrm{b,n+1}} \end{Bmatrix};\ d\dot{\boldsymbol{z}}_{\mathbf{n-1}} = \begin{Bmatrix} d\dot{z}_{\mathrm{g,n-1}} \\ d\dot{z}_{\mathrm{s,n-1}} \\ d\dot{z}_{\mathrm{b,n-1}} \end{Bmatrix};\ d\boldsymbol{z}_{\mathbf{n+1}} = \begin{Bmatrix} dz_{\mathrm{g,n+1}} \\ dz_{\mathrm{s,n+1}} \\ dz_{\mathrm{b,n+1}} \end{Bmatrix};\ d\boldsymbol{z}_{\mathbf{n-1}} = \begin{Bmatrix} dz_{\mathrm{g,n-1}} \\ dz_{\mathrm{s,n-1}} \\ dz_{\mathrm{b,n-1}} \end{Bmatrix} \tag{38}$$

$$d\dot{\boldsymbol{z}}^{\boldsymbol{p}}_{\mathbf{n+1}} = \begin{Bmatrix} d\dot{z}^{p}_{\mathrm{g,n+1}} \\ d\dot{z}^{p}_{\mathrm{s,n+1}} \\ d\dot{z}^{p}_{\mathrm{b,n+1}} \end{Bmatrix};\ d\dot{\boldsymbol{z}}^{\boldsymbol{p}}_{\mathbf{n-1}} = \begin{Bmatrix} d\dot{z}^{p}_{\mathrm{g,n-1}} \\ d\dot{z}^{p}_{\mathrm{s,n-1}} \\ d\dot{z}^{p}_{\mathrm{b,n-1}} \end{Bmatrix};\ d\boldsymbol{z}^{\boldsymbol{p}}_{\mathbf{n+1}} = \begin{Bmatrix} dz^{p}_{\mathrm{g,n+1}} \\ dz^{p}_{\mathrm{s,n+1}} \\ dz^{p}_{\mathrm{b,n+1}} \end{Bmatrix};\ d\boldsymbol{z}^{\boldsymbol{p}}_{\mathbf{n-1}} = \begin{Bmatrix} dz^{p}_{\mathrm{g,n-1}} \\ dz^{p}_{\mathrm{s,n-1}} \\ dz^{p}_{\mathrm{b,n-1}} \end{Bmatrix} \tag{39}$$

$$\boldsymbol{K} = \begin{bmatrix} k_{\mathrm{g}} + k_{\mathrm{s}} + 2k^{s}_{\mathrm{g}} & -k_{\mathrm{s}} & 0 \\ -k_{\mathrm{s}} & k_{\mathrm{s}} + k_{\mathrm{b}} + 2k^{s}_{\mathrm{s}} & -k_{\mathrm{b}} \\ 0 & -k_{\mathrm{b}} & k_{\mathrm{b}} + 2k^{s}_{\mathrm{b}} \end{bmatrix};\ \boldsymbol{K}^{\boldsymbol{p}} = \begin{bmatrix} -k_{\mathrm{g}} - 2k^{s}_{\mathrm{g}} & k_{\mathrm{s}} & 0 \\ -2k^{s}_{\mathrm{s}} & -k_{\mathrm{s}} - 2k^{s}_{\mathrm{s}} & k_{\mathrm{b}} \\ -2k^{s}_{\mathrm{b}} & -2k^{s}_{\mathrm{b}} & -k_{\mathrm{b}} - 2k^{s}_{\mathrm{b}} \end{bmatrix} \tag{40}$$

$$\boldsymbol{C} = \begin{bmatrix} c_{\mathrm{g}} + c_{\mathrm{s}} + 2c^{s}_{\mathrm{g}} & -c_{\mathrm{s}} & 0 \\ -c_{\mathrm{s}} & c_{\mathrm{s}} + c_{\mathrm{b}} + 2c^{s}_{\mathrm{s}} & -c_{\mathrm{b}} \\ 0 & -c_{\mathrm{b}} & c_{\mathrm{b}} + 2c^{s}_{\mathrm{b}} \end{bmatrix};\ \boldsymbol{C}^{\boldsymbol{p}} = \begin{bmatrix} -c_{\mathrm{g}} - 2c^{s}_{\mathrm{g}} & c_{\mathrm{s}} & 0 \\ -2c^{s}_{\mathrm{s}} & -c_{\mathrm{s}} - 2c^{s}_{\mathrm{s}} & c_{\mathrm{b}} \\ -2c^{s}_{\mathrm{b}} & -2c^{s}_{\mathrm{b}} & -c_{\mathrm{b}} - 2c^{s}_{\mathrm{b}} \end{bmatrix} \tag{41}$$

$$d\boldsymbol{F} = \begin{Bmatrix} dF_{\mathrm{g,n}} \\ dF_{\mathrm{s,n}} \\ dF_{\mathrm{b,n}} \end{Bmatrix};\ \boldsymbol{M} = \begin{bmatrix} m_{\mathrm{g}} & 0 & 0 \\ 0 & m_{\mathrm{s}} & 0 \\ 0 & 0 & m_{\mathrm{b}} \end{bmatrix};\ \boldsymbol{K}' = \begin{bmatrix} k^{s}_{\mathrm{g}} & 0 & 0 \\ 0 & k^{s}_{\mathrm{s}} & 0 \\ 0 & 0 & k^{s}_{\mathrm{b}} \end{bmatrix};\ \boldsymbol{K}^{\boldsymbol{p}'} = \begin{bmatrix} k^{s}_{\mathrm{g}} & 0 & 0 \\ k^{s}_{\mathrm{s}} & k^{s}_{\mathrm{s}} & 0 \\ k^{s}_{\mathrm{b}} & k^{s}_{\mathrm{b}} & k^{s}_{\mathrm{b}} \end{bmatrix};\ \boldsymbol{C}' = \begin{bmatrix} c^{s}_{\mathrm{g}} & 0 & 0 \\ 0 & c^{s}_{\mathrm{s}} & 0 \\ 0 & 0 & c^{s}_{\mathrm{b}} \end{bmatrix};\ \boldsymbol{C}^{\boldsymbol{p}'} = \begin{bmatrix} c^{s}_{\mathrm{g}} & 0 & 0 \\ c^{s}_{\mathrm{s}} & c^{s}_{\mathrm{s}} & 0 \\ c^{s}_{\mathrm{b}} & c^{s}_{\mathrm{b}} & c^{s}_{\mathrm{b}} \end{bmatrix} \tag{42}$$

FIGURE CAPTIONS

FIGURE 1 Deflection profile during the passage of train wheels

FIGURE 2 (a) Wheel load measured between adjacent sleepers[43]; (b) wheel load measured at sleeper location; (c) sleeper reaction force or rail seat load

FIGURE 3 Simplified geotechnical rheological model of the ballasted railway track

FIGURE 4 Effective region of the track substructure layers considered in the analysis

FIGURE 5 Generation of irrecoverable deformations during train-induced repeated loading

FIGURE 6 Comparison of the model predictions with the experimental results reported by Suiker et al.[60] for cyclic load tests on ballast: variation of deviatoric strain with the number of load cycles at confining pressure of (a) 41.3 kPa; (b) 68.9 kPa

FIGURE 7 Comparison of the model predictions with the experimental results reported by Suiker et al.[60] for cyclic load tests on subballast: variation of deviatoric strain with the number of load cycles at confining pressure of (a) 41.3 kPa; (b) 68.9 kPa

FIGURE 8 Comparison of the experimental results for soil reported by Wichtmann[66] with the model predictions: (a) stress-strain curve; (b) variation of axial strain with the number of load cycles (solid lines and symbols represent model predictions and experimental data, respectively)

FIGURE 9 Flowchart to predict the track response under train-induced repeated loads

FIGURE 10 Comparison of data reported by Gräbe et al.[68] with predicted results: (a) variation of vertical stress with time (solid and dotted lines represent model predictions and in-situ measurements, respectively); (b) variation of vertical resilient deformation with depth

FIGURE 11 Comparison of data reported by Priest et al.[13] with predicted results: (a) variation of vertical displacement of sleeper with time; (b) variation of the increase in vertical and horizontal stresses at 800 mm below sleeper bottom with time

FIGURE 12 Comparison of cumulative irrecoverable deformation recorded by Gräbe and Shaw[69] with model predictions

FIGURE 13 Vertical stress distribution with depth under different axle loads

FIGURE 14 Distribution of settlement accumulated after a cumulative tonnage of 20 MGT with depth under different axle loads

FIGURE 15 Distribution of settlement accumulated after a cumulative tonnage of 25 MGT with depth under different train speeds

FIGURE 16 Variation of subgrade settlement with tonnage at different granular layer thickness

FIGURE 17 Variation of settlement accumulated after a cumulative tonnage of 25 MGT, with granular layer thickness, for (a) subgrade; (b) granular layers

FIGURE A1 Transfer of train-induced load from superstructure to the substructure layers

LIST OF TABLES

TABLE 1 Constitutive parameters for the plastic slider element for granular layers

	Suiker et al.[60]		Gräbe and Shaw[69]
Parameter	**Ballast**	**Subballast**	**Engineered fill**
Γ	1.4	0.9	0.9
λ	0.1	0.05	0.05
M_{tc}	1.25	1.15	1.25
N_v	0.2	0.3	0.3
χ_{tc}	3	4.2	4.5
a_h	0.143	0.185	0.175
H	50–250ψ	160–260ψ	7600–1000ψ

TABLE 2 Model parameters for the plastic slider element for subgrade soil

Reference	e_0	λ	κ	φ_c (°)	ξ	A	a_h
Wichtmann[66]	0.7	0.0046	0.0009	31.2	0.1	0.31	0.0135
Gräbe and Shaw[69]	0.3	0.0022	0.002	51	0.45	0.02	0.075

TABLE 3 Parameters for the simulation of viscoelasto-plastic track response

Variable	Symbol	Unit	Priest et al.[13], Gräbe et al.[68], Gräbe and Shaw[69]	Present study
Ballast (Layer 1)				
Young's modulus	E_b	MPa	100	276
Poisson's ratio	ν_b	–	0.3	0.3
Shear stiffness	k_b^s	MN/m	0.1	78.4
Shear damping	c_b^s	kNs/m	80	80
Density	ρ_b	kg/m^3	1800	1760
Thickness	h_b	m	0.3	0.3 – 0.75 (0.3)
Subballast (Layer 2)				
Young's modulus	E_s	MPa	220	115
Poisson's ratio	ν_s	–	0.3	0.4
Shear stiffness	k_s^s	MN/m	476	476
Shear damping	c_s^s	kNs/m	80	80
Density	ρ_s	kg/m^3	2175	1920
Thickness	h_s	m	0.8	0.15 – 0.6 (0.15)
Subgrade				
Young's modulus	E_g	MPa	27000	20
Poisson's ratio	ν_g	–	0.25	0.45
Shear stiffness	k_g^s	MN/m	1600	1600
Shear damping	c_g^s	kNs/m	80	80
Density	ρ_g	kg/m^3	2300	1920
Thickness	h_g	m	3.29	10

Note: The shear damping and shear stiffness values are derived using an optimisation technique in which, the range of variation was selected based on the values reported by Zhai et al.[34] and Oscarsson and Dahlberg[75].

NOTATIONS

a = equivalent radius of sleeper-ballast contact area (m);
a_h = cyclic hardening parameter;
a_t = number of wheels or axles considered;
c_b, c_s, c_g = viscous damping coefficients for ballast, subballast and subgrade, respectively (Ns/m);
c^s_b, c^s_s, c^s_g = shear damping coefficients for ballast, subballast and subgrade, respectively (Ns/m);
D = dilatancy;
$dF_{g,n}$, $dF_{s,n}$, $dF_{b,n}$ = external force increment acting on subgrade, subballast and ballast layers, respectively (N);
D_p = plastic dilatancy;
D_w = train wheel diameter (m);
$\mathrm{d}p_i$ = image mean effective stress increment (N/m^2);
$\mathrm{d}t$ = time step (s);
e, e_0 = current and initial void ratio, respectively;
e_c = void ratio on the critical state line at the current mean effective stress;
E_r, E_b, E_s, E_g = Young's modulus of rail, ballast, subballast and subgrade, respectively (N/m^2);
f_g, f_s, f_b = yield surface for subgrade, subballast and ballast, respectively;
f_c, f_r, f_t = current, reference and transitional surfaces, respectively;
g = potential function;
H, p_{ic}, p_{im}, R_i = hardening parameters;
h_b, h_s, h_g = ballast, subballast and subgrade thickness, respectively (m);
h_{eb}, h_{es} = equivalent thickness of ballast and subballast layers, respectively (m);
h_{gl} = granular layer thickness (m);
i_1, i_2 = empirical parameters used for the calculation of dynamic amplification factor;
I_r = moment of inertia of rail (m^4);
k = track modulus (N/m^2);
k_b, k_s, k_g = stiffness of ballast, subballast and subgrade, respectively (N/m);
k_p, k_t = stiffness of rail pad and system support stiffness, respectively (N/m);
k^s_b, k^s_s, k^s_g = shear stiffness of ballast, subballast and subgrade, respectively (N/m);
L = characteristic length (m);
M = critical stress ratio;
m_b, m_s, m_g = vibrating mass of ballast, subballast and subgrade, respectively (kg);
M_i = critical stress ratio corresponding to image state;
M_{itc} = critical stress ratio corresponding to the image state for triaxial compression;
M_{tc} = critical stress ratio under triaxial compression;
N_v = volumetric coupling coefficient;
N = number of load cycles;
p = mean effective stress (N/m^2);
p_i = image mean effective stress (N/m^2);
q = deviatoric stress (N/m^2);
Q, Q_a = static wheel and axle load, respectively (N);
$Q_{r,n}$ = vertical rail seat load at n^{th} sleeper (N);
R = parameter that controls the magnitude of plastic volumetric strain increment;
S_s = sleeper spacing (m);
s_g, s_{gl} = settlement of subgrade and granular layers, respectively (m);
$\boldsymbol{s}_{ij}$ = deviatoric stress tensor;
s_t = settlement of track substructure (m);
s_v^r = vertical resilient deformation (m);

t = time instant (s);
V = train speed (km/h);
w = vertical track deflection (m);
x_n^j = distance of n^{th} sleeper from j^{th} wheel/axle (m);
$z_{b,n}$, $\dot{z}_{b,n}$, $\ddot{z}_{b,n}$ = displacement, velocity and acceleration of ballast below n^{th} sleeper, respectively;
$z_{s,n}$, $\dot{z}_{s,n}$, $\ddot{z}_{s,n}$ = displacement, velocity and acceleration of subballast below n^{th} sleeper, respectively;
$z^p_{b,n}$, $\dot{z}^p_{b,n}$ = plastic displacement and velocity of ballast below n^{th} sleeper, respectively;
$z^p_{s,n}$, $\dot{z}^p_{s,n}$ = plastic displacement and velocity of subballast below n^{th} sleeper, respectively;
$z^p_{g,n}$, $\dot{z}^p_{g,n}$ = plastic displacement and velocity of subgrade below n^{th} sleeper, respectively;
$z_{g,n}$, $\dot{z}_{g,n}$, $\ddot{z}_{g,n}$ = displacement, velocity and acceleration of subgrade below n^{th} sleeper, respectively;
z_g^{ve}, z_s^{ve}, z_b^{ve} = visco-elastic displacement in subgrade, subballast and ballast, respectively;
z = depth (m);
α, β, γ = stress distribution angles for ballast, subballast and subgrade, respectively (°);
δ_{ij} = Kronecker delta;
$d\hat{p}$, $d\hat{q}$ = hydrostatic and deviatoric stress increments in characteristic stress space, respectively;
$d\varepsilon_v$, $d\varepsilon_q$ = volumetric and deviatoric strain increments, respectively;
$d\varepsilon^p_{ij}$, ε^p_v = plastic strain increment and cumulative plastic volumetric strain, respectively;
$d\varepsilon^p_v$, $d\varepsilon^p_q$ = plastic volumetric and deviatoric strain increments, respectively;
$d\varepsilon^p_z$ = plastic strain increment in vertical direction;
$\Delta\sigma$ = increase in stress (N/m^2);
ε_a = axial strain;
ε_a^p = accumulated axial strain;
ε_q = deviatoric strain;
Γ = critical void ratio at p = 1 kPa;
$\hat{\Gamma}$, $\hat{N}$ = void ratio of critical state line and normal compression line at $\hat{p}$=1 kPa, respectively;
η = stress ratio;
$\mathcal{J}$ = tensorial invariant;
$\hat{\eta}$ = stress ratio in characteristic stress space;
Λ_s, Λ_g = scalars;
λ, κ = slope of critical state line and swelling line in e–ln p space, respectively;
$\hat{M}$ = critical stress ratio in characteristic stress space;
$\hat{p}_{xg}$ = intersection of potential function with $\hat{p}$ axis;
$\hat{p}_{xt}$, $\hat{p}_{xc}$, $\hat{p}_{xr}$ = intersection of transitional, current and reference surfaces with $\hat{p}$ axis, respectively;
$\hat{q}$ and $\hat{p}$ = deviatoric and hydrostatic stress invariants in the characteristic stress space, respectively;
ν_b, ν_s, ν_g = Poisson's ratio of ballast, subballast and subgrade, respectively;
ξ, A = dimensionless material parameters;
ρ_b, ρ_s, ρ_g = density of ballast, subballast and subgrade, respectively (kg/m^3);
σ_{sb}, σ_{bs}, σ_{sg}, σ_{go} = vertical stresses at the sleeper-ballast, ballast-subballast, subballast-subgrade interfaces and bottom of subgrade layer, respectively (N/m^2);
σ_c = confining pressure in triaxial tests (N/m^2);
$\boldsymbol{\sigma}_{ij}$ = stress tensor;
σ_j = principal stress (N/m^2);
σ_{ref} = reference stress (N/m^2);

σ_v = vertical stress (N/m^2);

$\hat{\sigma}_{ij}$ = characteristic stress tensor;

φ_c, φ_e = critical state friction angles under triaxial compression and extension tests, respectively (°);

χ_i, χ_{tc} = dilatancy parameter corresponding to image state and triaxial compression, respectively;

ψ = state parameter;

ψ_i = image state parameter;

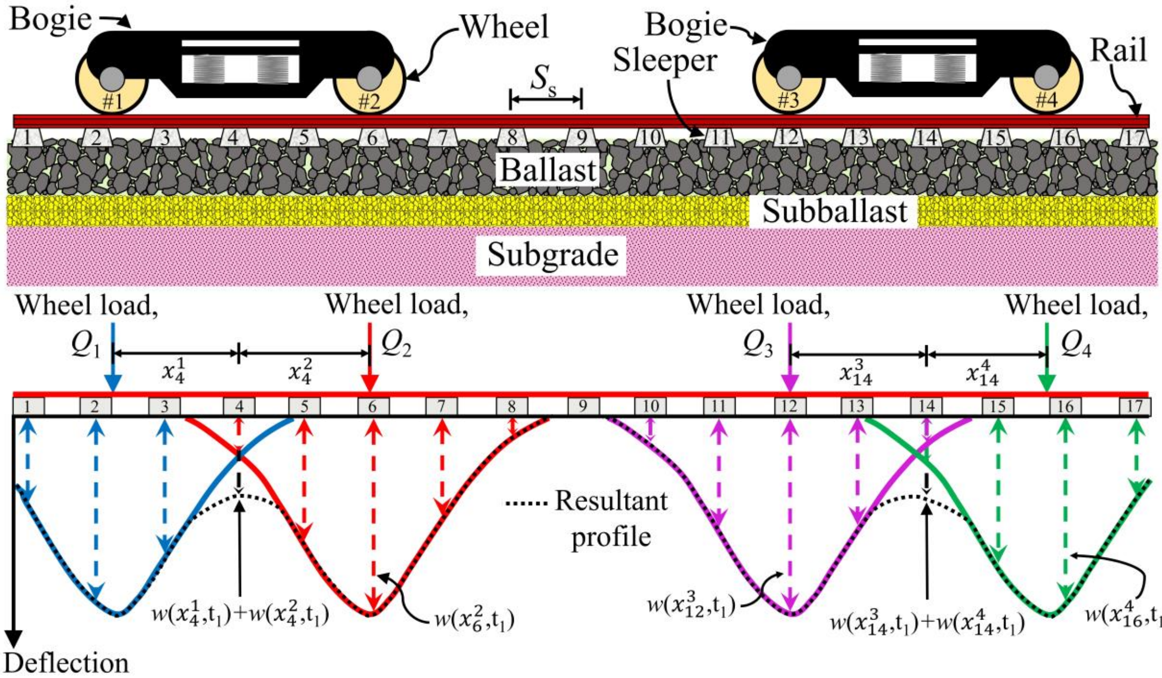

FIGURE 1 Deflection profile during the passage of train wheels

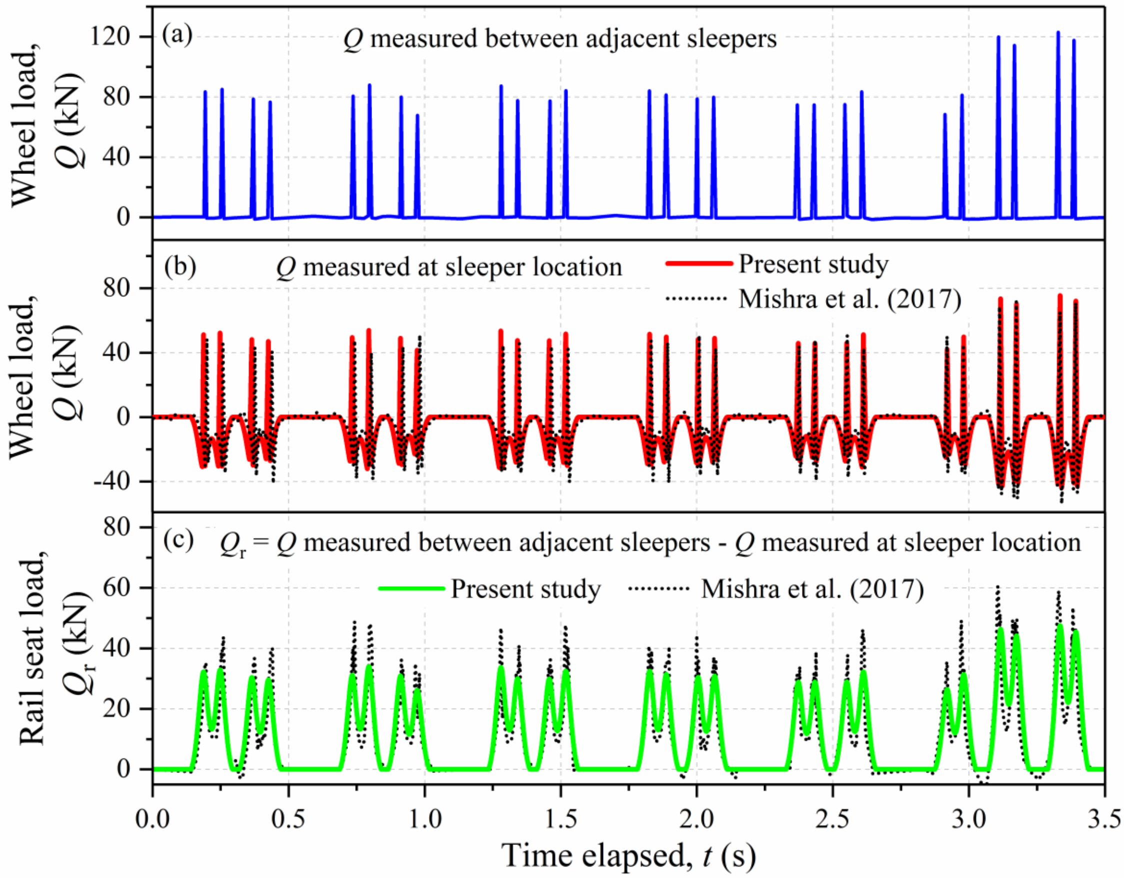

FIGURE 2(a) Wheel load measured between adjacent sleepers[43]; (b) wheel load measured at sleeper location; (c) sleeper reaction force or rail seat load

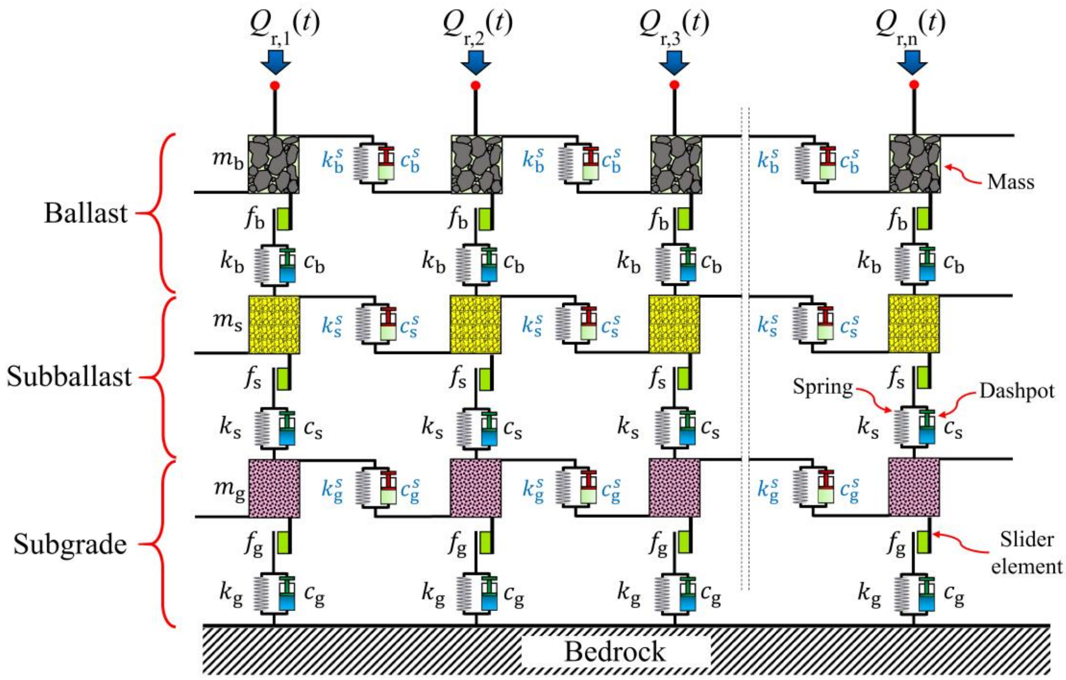

FIGURE 3 Simplified geotechnical rheological model of the ballasted railway track

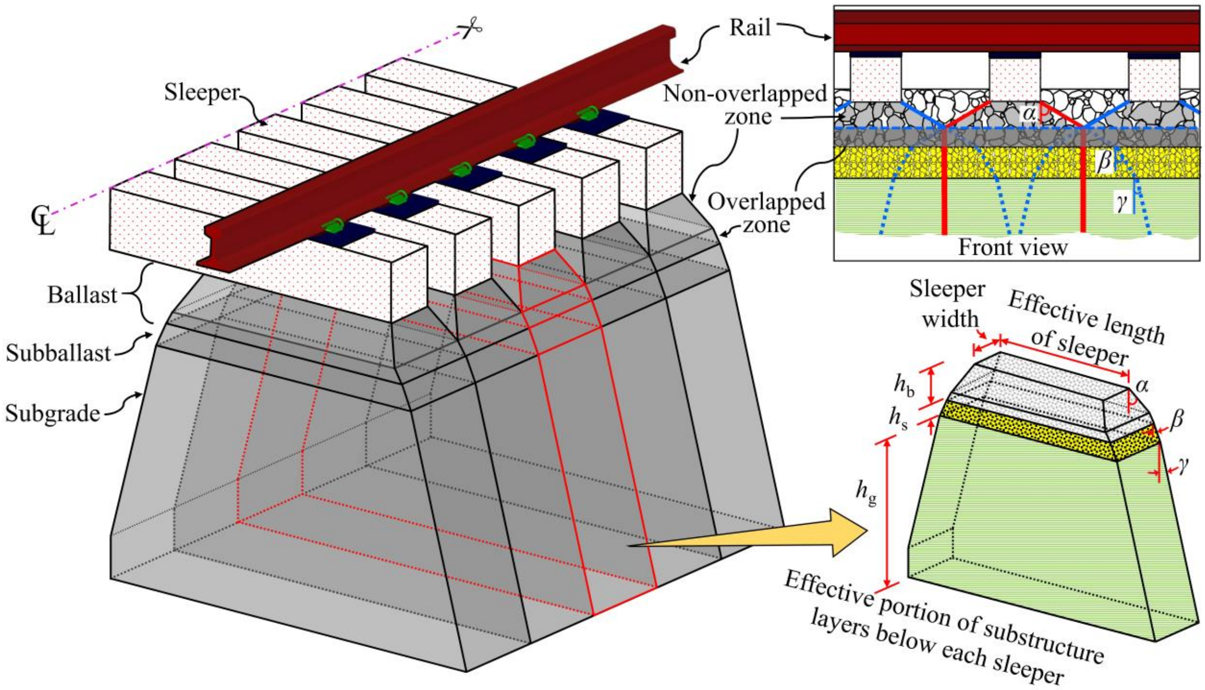

FIGURE 4 Effective region of the track substructure layers considered in the analysis

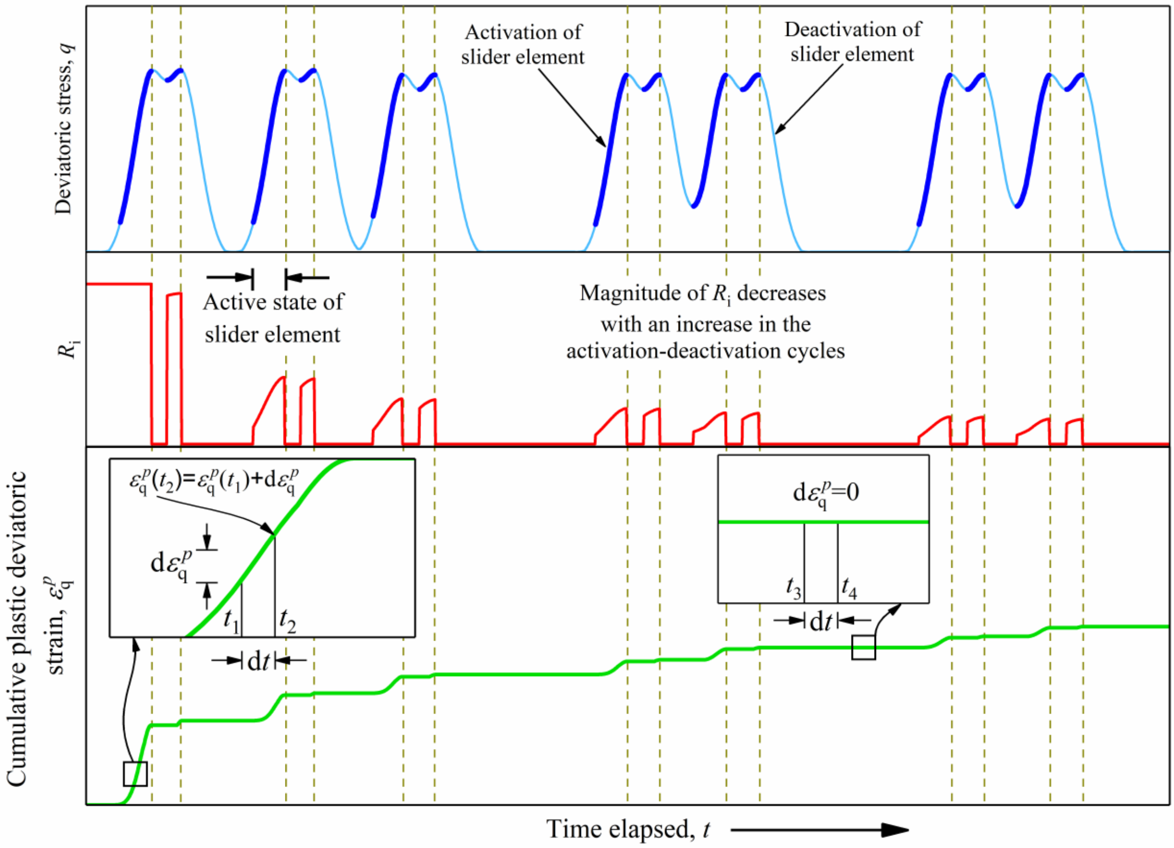

FIGURE 5 Generation of irrecoverable deformations during train-induced repeated loading

975

976

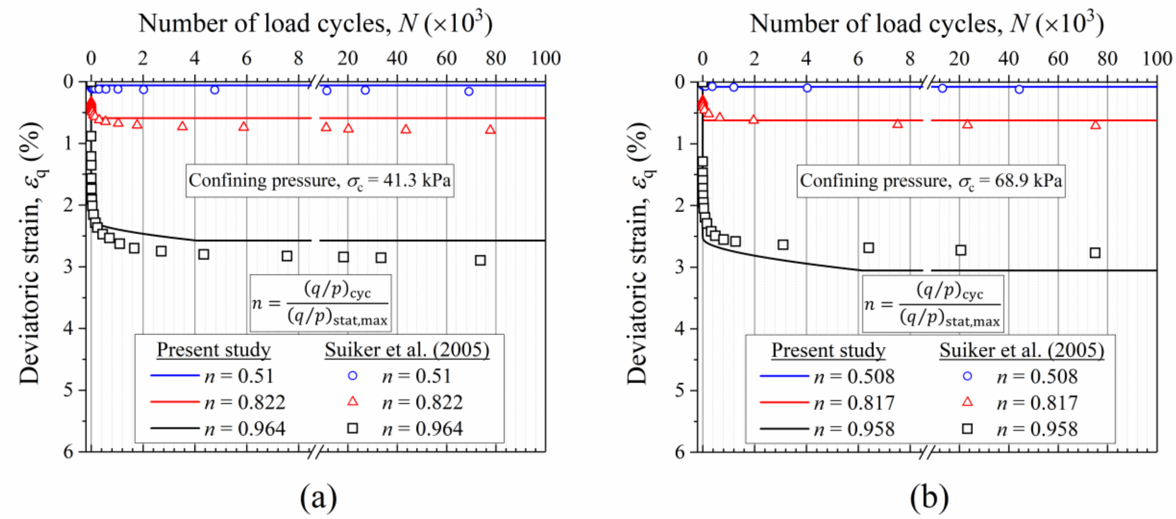

FIGURE 6 Comparison of the model predictions with the experimental results reported by Suiker et al.[60] for cyclic load tests on ballast; variation of deviatoric strain with the number of load cycles at confining pressure of (a) 41.3 kPa; (b) 68.9 kPa

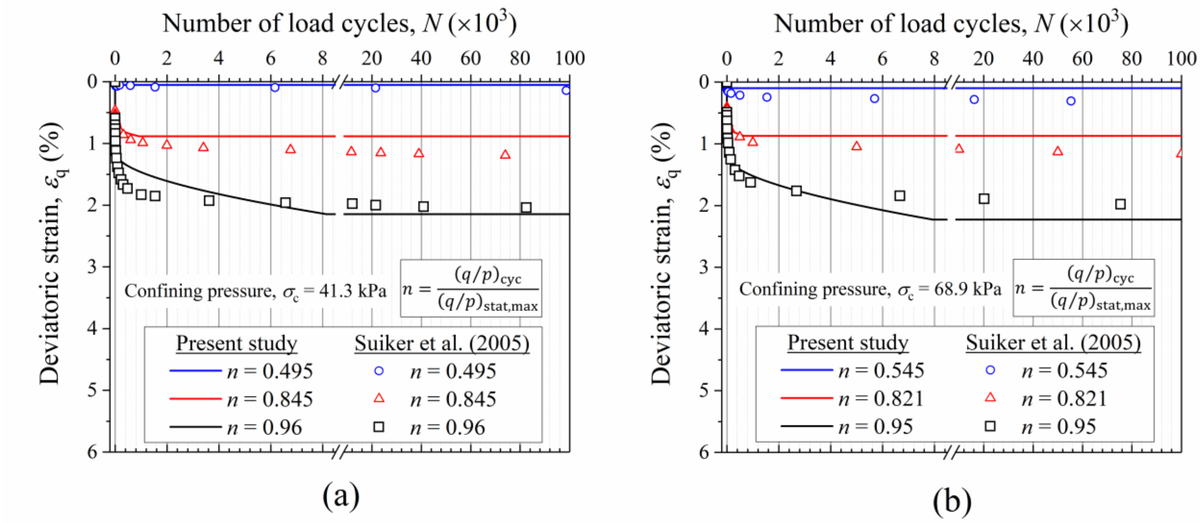

FIGURE 7 Comparison of the model predictions with the experimental results reported by Suiker et al.[60] for cyclic load tests on subballast: variation of deviatoric strain with the number of load cycles at confining pressure of (a) 41.3 kPa; (b) 68.9 kPa

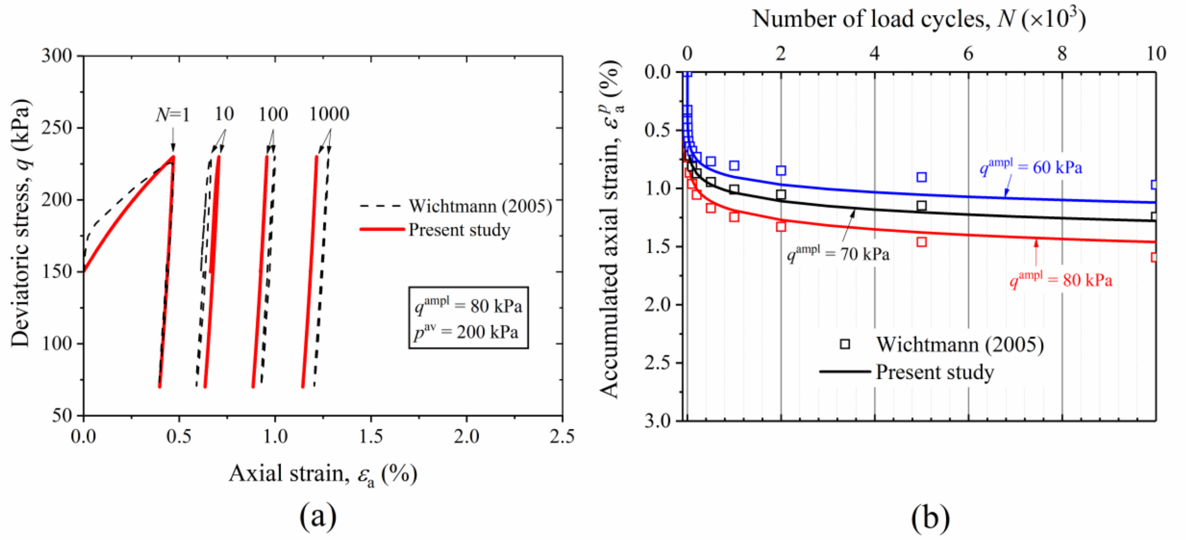

FIGURE 8 Comparison of the experimental results for soil reported by Wichtmann[66] with the model predictions: (a) stress-strain curve; (b) variation of axial strain with the number of load cycles (solid lines and symbols represent model predictions and experimental data, respectively)

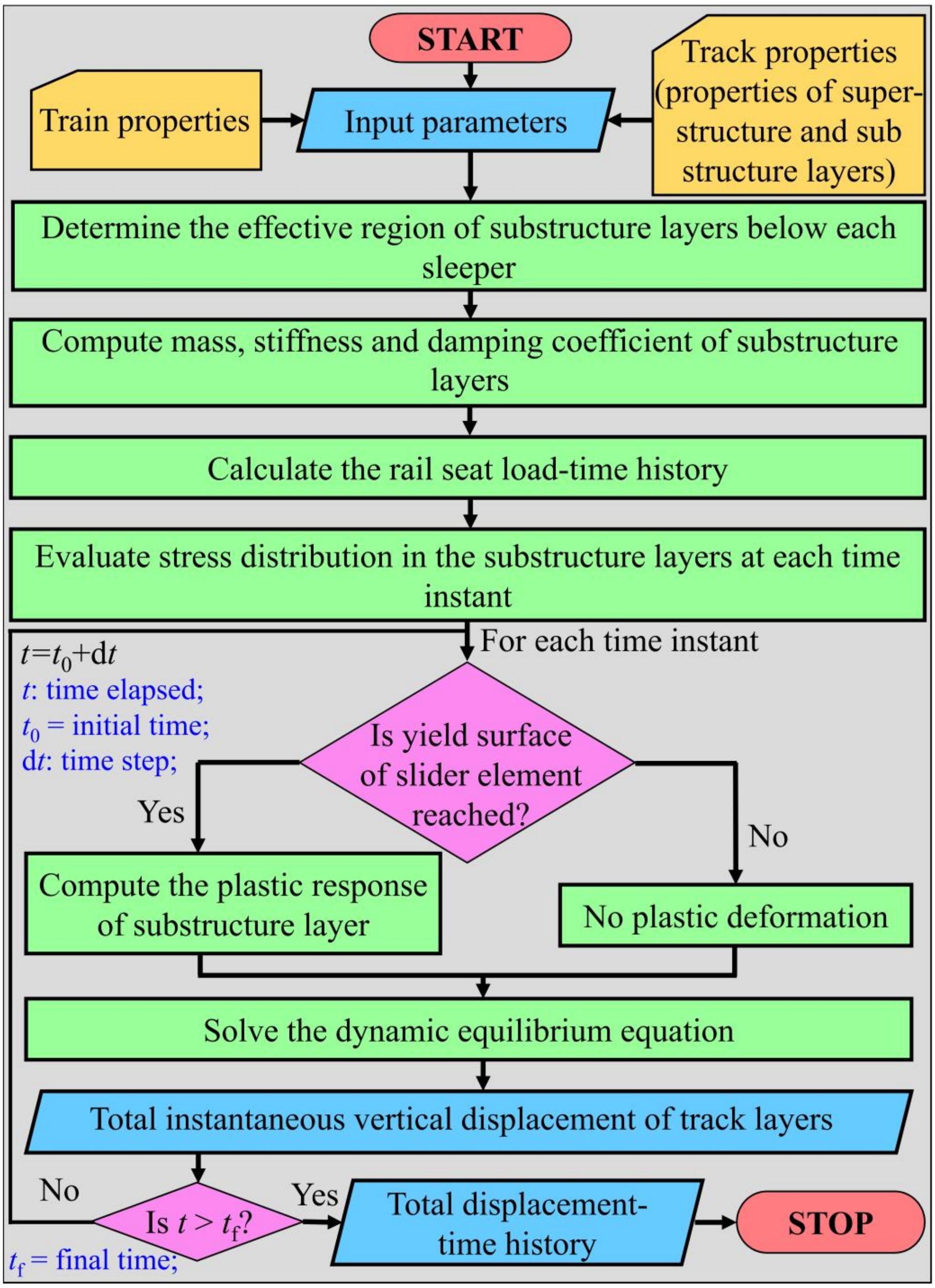

FIGURE 9 Flowchart to predict the track response under train-induced repeated loads

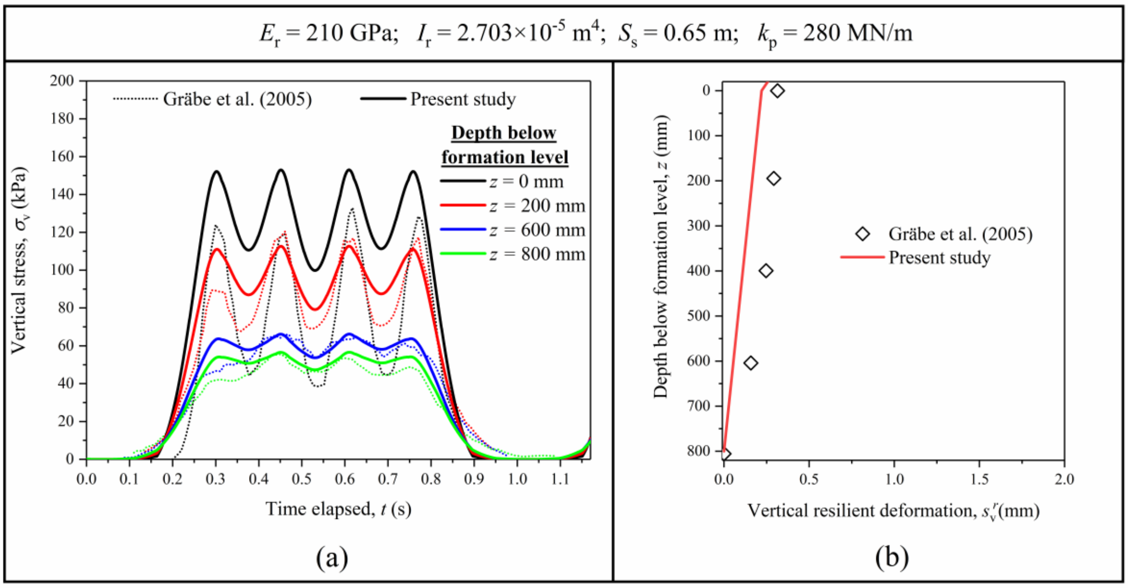

FIGURE 10 Comparison of data reported by Gräbe et al.[68] with predicted results: (a) variation of vertical stress with time (solid and dotted lines represent model predictions and in-situ measurements, respectively); (b) variation of vertical resilient deformation with depth

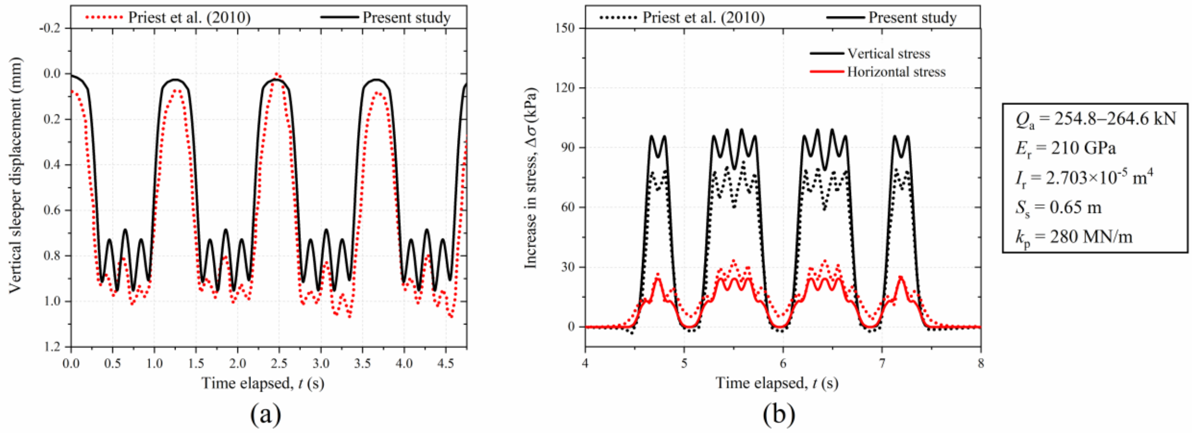

FIGURE 11 Comparison of data reported by Priest et al.[13] with predicted results: (a) variation of vertical displacement of sleeper with time; (b) variation of the increase in vertical and horizontal stresses at 800 mm below sleeper bottom with time

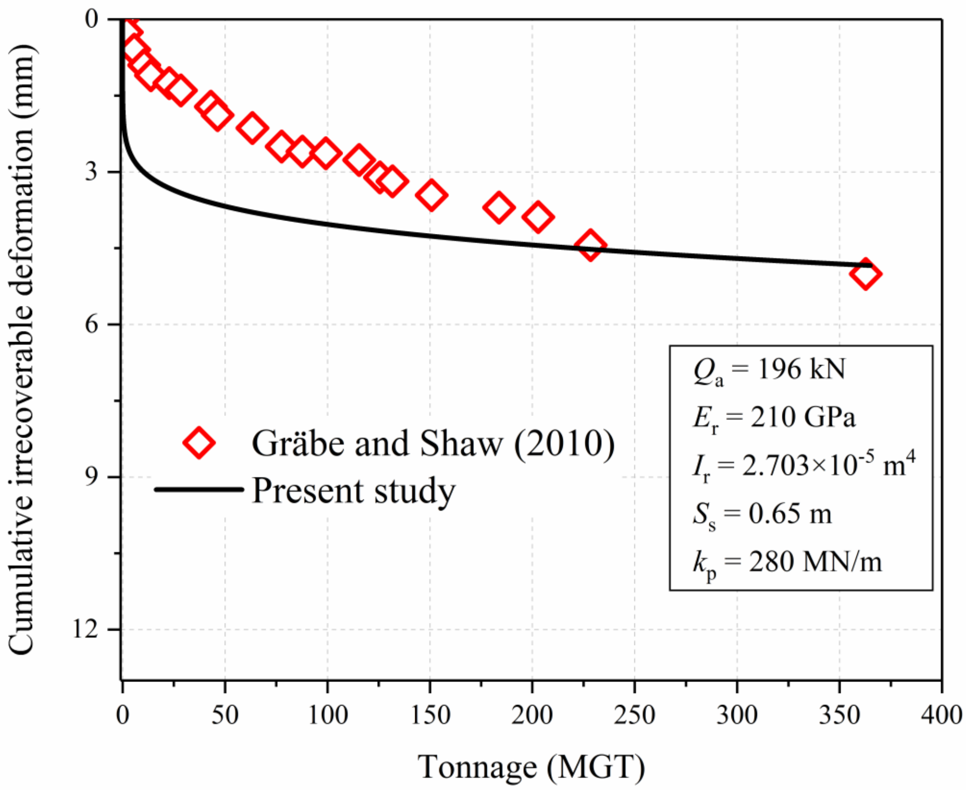

FIGURE 12 Comparison of cumulative irrecoverable deformation recorded by Gräbe and Shaw[69] with model predictions

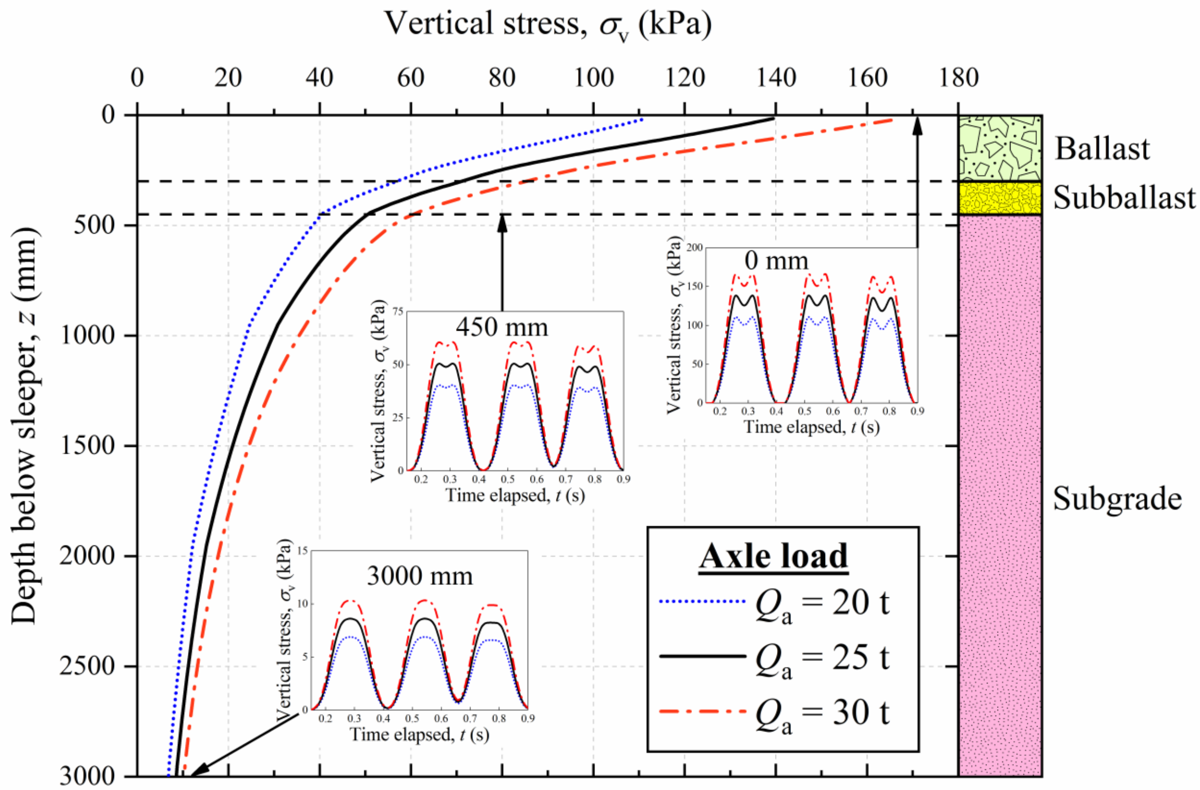

FIGURE 13 Vertical stress distribution with depth under different axle loads

991

992

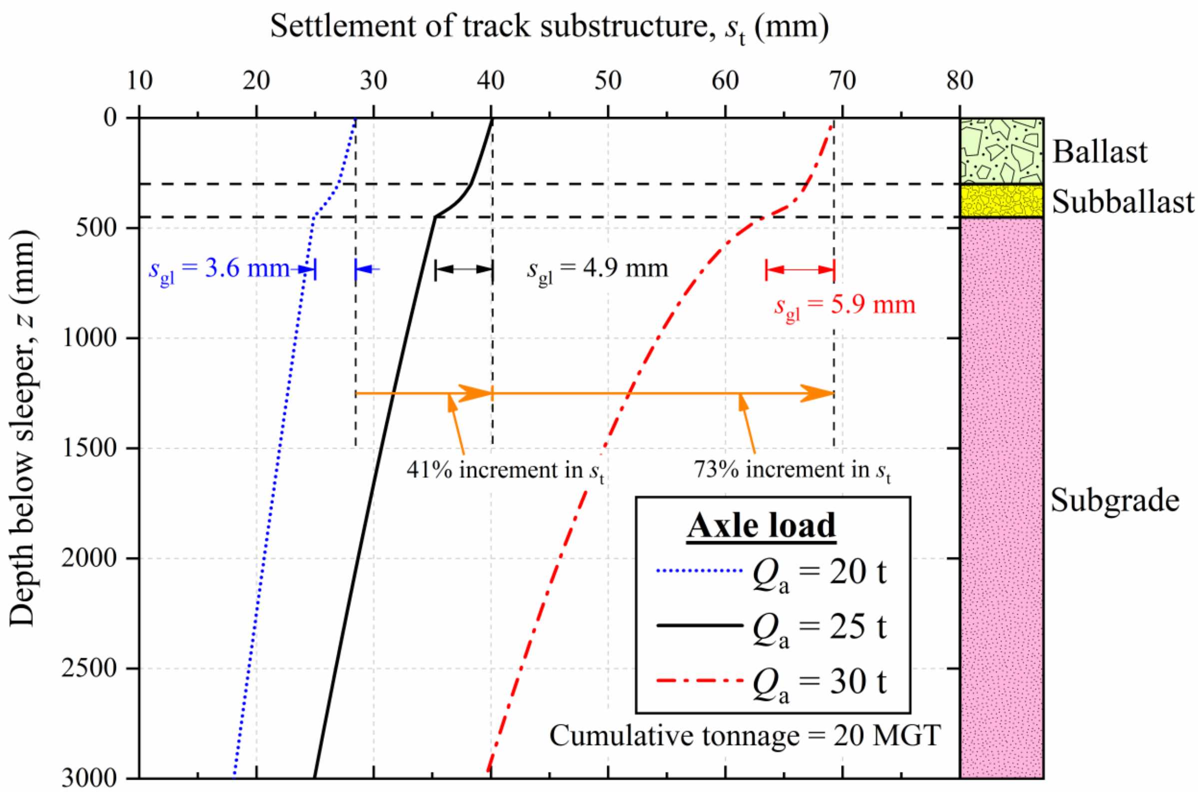

FIGURE 14 Distribution of settlement accumulated after a cumulative tonnage of 20 MGT with depth under different axle loads

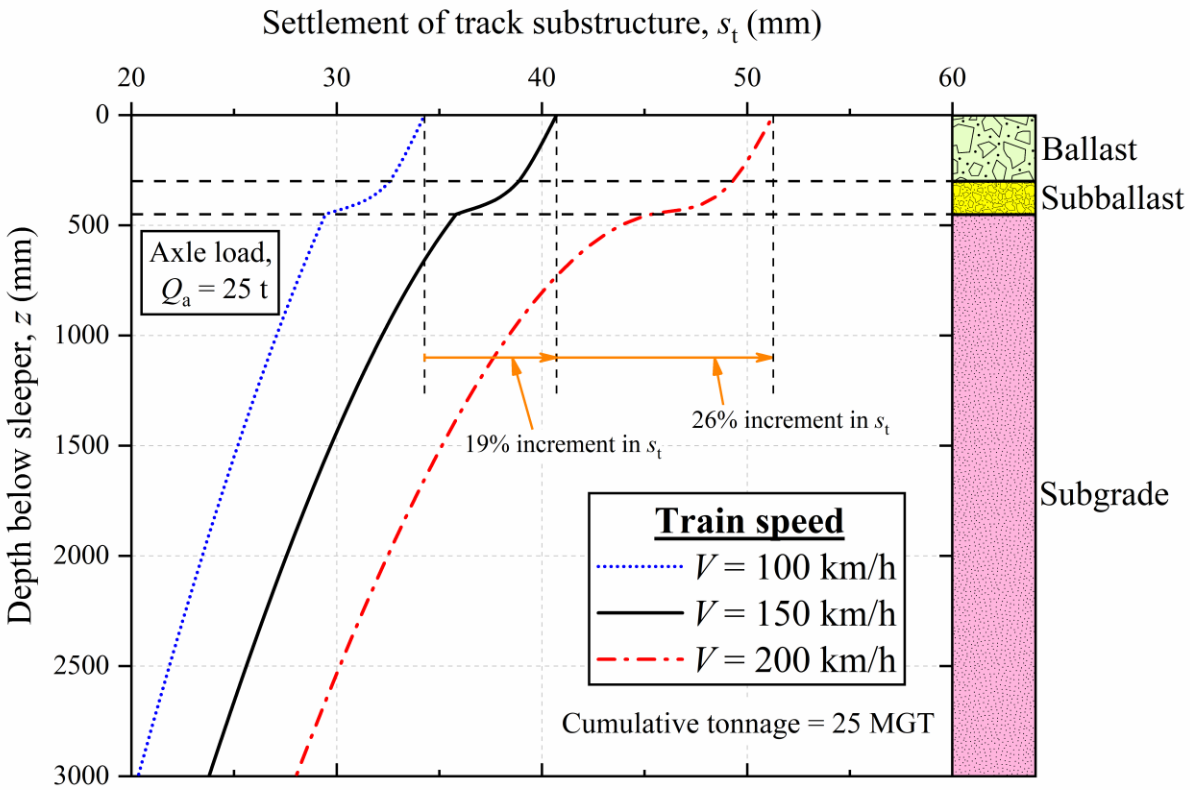

FIGURE 15 Distribution of settlement accumulated after a cumulative tonnage of 25 MGT with depth under different train speeds

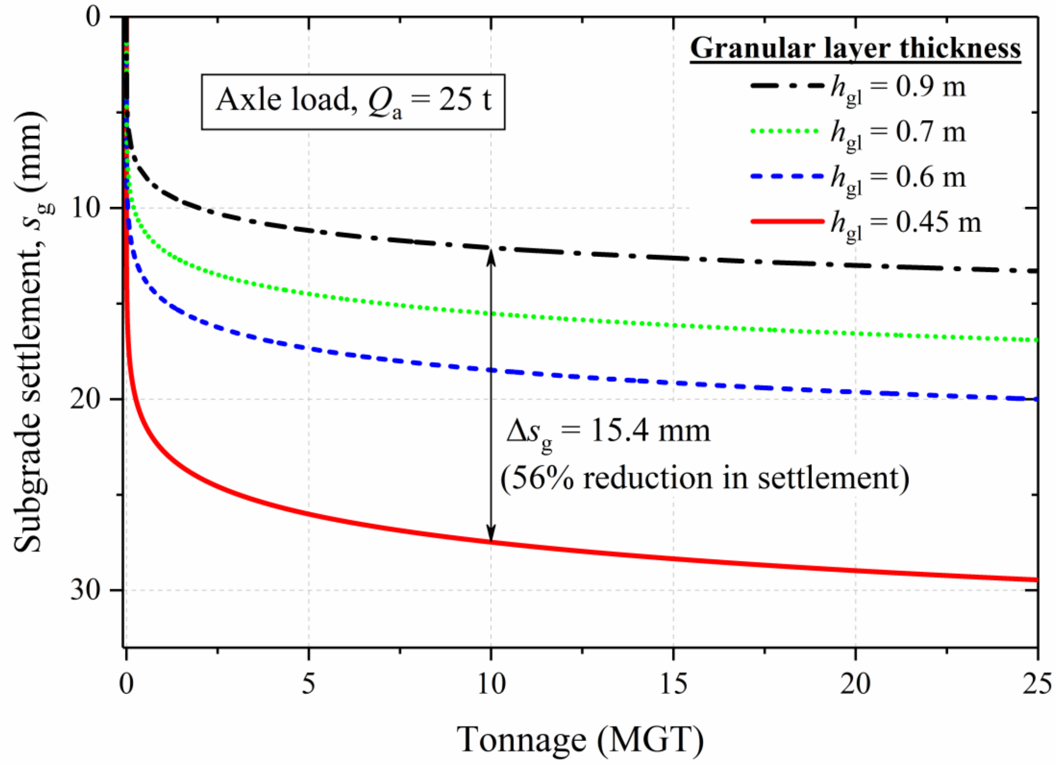

FIGURE 16 Variation of subgrade settlement with tonnage at different granular layer thickness

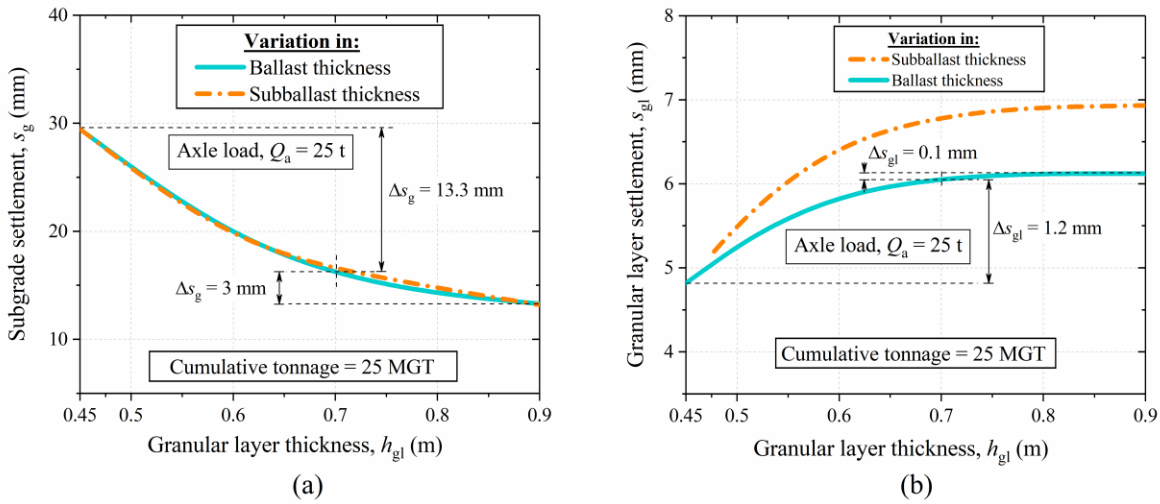

FIGURE 17 Variation of settlement accumulated after a cumulative tonnage of 25 MGT, with granular layer thickness, for (a) subgrade; (b) granular layers

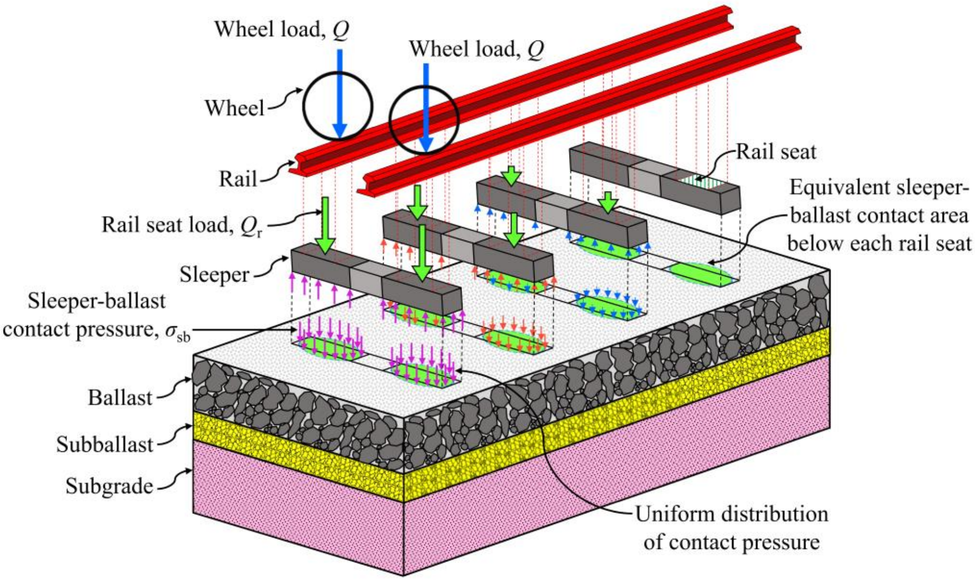

FIGURE A1 Transfer of train-induced load from superstructure to the substructure layers

1001